Politecnico di Torino
Imperial College London

Master's Degree in Aerospace Engineering

Politecnico di Torino

IMPERIAL

Master's Thesis in Aerospace Engineering

Innovating Aero-Engine Dynamics: Numerical Modelling of Wave Propagation in Granular Crystal

Supervisors

Prof. Daniele Botto
Dr. Alfredo Fantetti

Candidate

Filippo Vergnano

Academic Year 2025/2026
March 2026

Acknowledgements

I would like to thank my family from the bottom of my heart for always being the hand supporting me, for standing by me through every step and for being an inspiring example I can always look up to

I would like to thank Dr. Alfredo Fantetti, my supervisor at Imperial College, for guiding me through this research and for teaching me a new perspective with which to view things.

I would like to thank Jaffry Jaman for accompanying me throughout this research.

I would like to thank Professor Daniele Botto, my supervisor at Politecnico di Torino, for giving me the opportunity to undertake this experience and for patiently supervising me throughout this thesis journey.

Finally, thanks to all the people who have stood by me during my university studies; your friendship and support have always been a great motivation for me.

Abstract

The aviation sector faces the continuous challenge of developing efficient engines and lightweight structures. However, reducing structural weight often increases system vibrations, which can affect performance and structural integrity. Frictional joints are commonly employed to mitigate these vibrations, yet their effectiveness strongly depends on the contact conditions at the interface. This motivates the development of experimental techniques for interface characterization and structural health monitoring.

Among the existing experimental techniques, solitary waves, i.e., mechanical waves similar to ultrasonic waves that propagate in ordered chains of spheres named granular chains, have shown potential as a tool for detecting physical properties such as thickness and elastic modulus in components. At Imperial College, where I performed my research, such waves are being used for contact analysis, since their propagation speed depends on the properties of the contact interfaces.

The present thesis focuses on the numerical modeling of solitary waves interacting with a steel block in a dedicated experimental setup.

The objective is to accurately reproduce the existing experimental data of reflected solitary waves, providing a fundamental reference configuration for future investigations on the experimental setup. Specifically, an existing MATLAB code for the propagation of solitary waves has been upgraded to model the interaction of the solitary wave with the steel block. Three modeling approaches were considered to represent different block behaviors and to identify the configuration that best matches the experimental data: 1) a rigid fixed-wall assumption, 2) a single-degree-of-freedom dynamic system, and 3) a high-fidelity wall model developed in Abaqus, for which a Reduced Order Model was implemented to integrate its dynamic response into the MATLAB simulation framework.

Simulations show that the system response is significantly influenced by the dynamic behavior of the block, especially in the secondary solitary wave reflections, which propagate through subsequent chain–wall interactions. This work provides the foundation for the future development of a non-destructive evaluation tool based on solitary waves for the characterization of contact states across an interface.

Contents

List of Figures

List of Tables

Acronyms

SW	Solitary Wave
RSW	Reflected Solitary Wave
DOF	Degree of Freedom
FEM	Finite Element Method
ROM	Reduced Order Model
DEM	Discrete Element Method
ODE	Ordinary Differential Equation
FFT	Fast Fourier Transform

Chapter 1

Introduction

Contact mechanics covers a wide range of engineering applications, from the automotive to the aerospace industries. Engineering structures such as aero-engines are composed of thousands of mechanical components due to their complex geometry and demanding operating conditions. These components are often connected through friction joints (fig.1.1), which not only provide structural integrity but also contribute to vibration damping. However, friction joints are challenging to model due to the lack of experimental data, which limits the predictive capabilities to track their complex contact states such as stick, micro-slip, gross-slip and separation condition.

In recent years, numerous studies have proposed different innovative approaches for monitoring frictional contacts such as optical measurements, ultrasound waves, and solitary waves. Among these techniques, the use of optical measurements represents a valid method only when at least one of the contacting components has transparent properties, which significantly restrict their applicability in industrial and aerospace environments. Ultrasonic waves, on the other hand, enable the characterization of metallic contact interfaces by evaluating the amount of energy transmitted and reflected at the interface. This method is applicable to a wider range of operating conditions than optical techniques. However, a major limitation of this technique is that the output signal is strongly affected by external disturbances in complex structures, such as aircraft engines, where multiple sources of vibration and noise are present.

Unlike sound waves, solitary waves are compactly supported nonlinear waves generated in granular crystals, which are arrays of spherical particles. Solitary waves exhibit unique properties: they can support high levels of acoustic energy within a fixed wavelength, and their propagation speed can be tuned by varying the granular crystal system's parameters (material properties, applied pre-compression and

geometry). This characteristics make solitary waves a potential opportunity for a breakthrough in the key industrial challenge of designing jointed structures that can mitigate vibrations whilst simultaneously ensuring that frictional wear occurs at most in less critical regions.
Solitary waves have been employed in an innovative experimental test rig developed through a collaboration between the University of Illinois at Urbana–Champaign and Imperial College London. The purpose of this apparatus is to investigate the frictional state of a mechanical contact between a steel assembly and a steel sphere.

The ultimate goal of this research is the development of a non-destructive evaluation (NDE) tool based on a hammer composed of spherical particles, capable of extracting information about the internal structure of materials and the frictional conditions of mechanical contacts.
This Master's thesis focuses on the study, modeling, and validation of such a system. The main objectives of the project can be summarized as follows:

1. To study the generation and propagation of solitary waves in granular crystals.
2. To improve a numerical model of a test rig based on solitary wave dynamics.
3. To implement and analyze different wall boundary conditions within the numerical model.
4. To validate the numerical model by matching experimental data, enabling its use as a characterization tool for the development of the non-destructive evaluation technique.

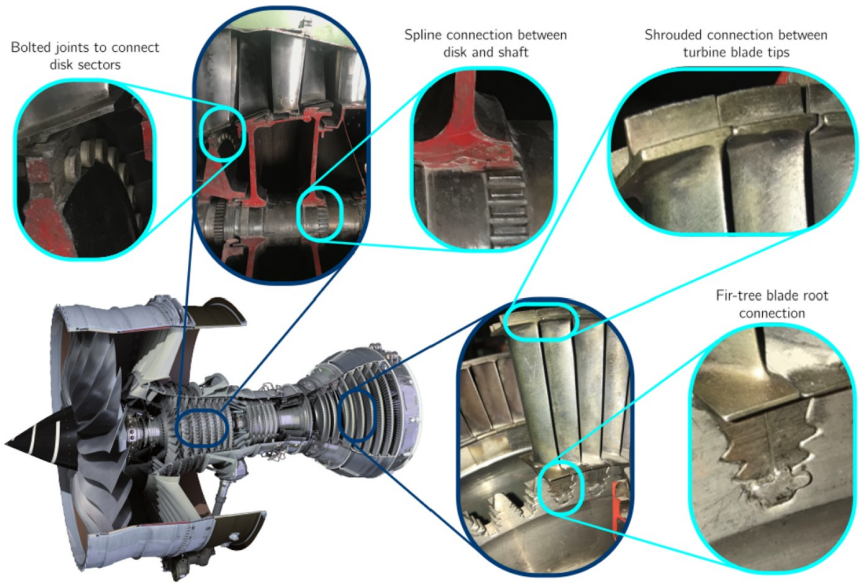

Figure 1.1: Typical jointed structures found in aeroengines. Taken from [1]

Chapter 2

Theoretical Background

In the context of this work, granular systems are composed of discrete, linearly elastic, spherical particles interacting through strongly nonlinear Hertzian contacts. The interest in studying these materials arises from their highly nonlinear dynamics, which lead to adaptive and tailorable dynamical properties [4]. In recent years, numerous studies have investigated wave propagation in one-dimensional granular systems, leading to the discovery of solitary waves.
Solitary waves (SW) are lumps of energy that present unique scattering and superposition response. They are characterized by a compactly supported shape and extremely slow propagation speed in comparison to the sound speed of the material that composes the partcles in the chain [3]. The propagation of these SWs is attributed to the counterbalancing of dispersion and strong nonlinearity effects due to Hertzian law interaction between beads [4]. In a chain of granular crystals, traveling waves form in the wake of a propagating pulse due to continuous scattering at the interfaces between adjacent beads.

Figure 2.1: Newton's craddle: example of granular chain

To fully understand the nonlinearity of these waves, it is essential to consider

Hertz's contact law, which provides the most accurate approximation of particle interactions.

2.1 Hertz theory

When two non-conforming bodies, such as two spheres or a sphere and a flat surface, are brought into contact they touch initially at a single point. Under the action of the slightest load they deform in the vicinity of their point of first contact so that they touch over an area which is finite though small compared with the dimensions of the two bodies [2].

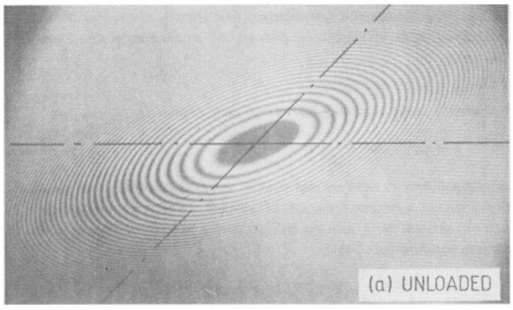

Figure 2.2: **(a)**

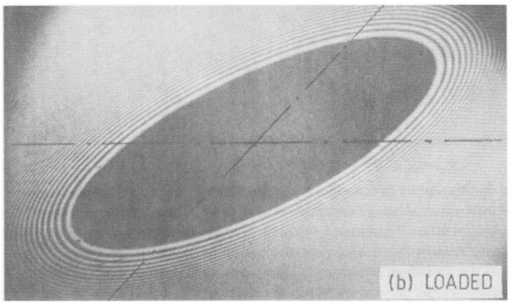

Figure 2.3: **(b)**

Figure 2.4: Contact area between two spheres before and after the application of a load. Taken from [2]

In 1882 Hertz defined a theory that well described the contact between two non-conformal bodies. His main focus was on calculating local deformations rather than the overall stress distribution, which depends on the shape of the bodies and their support conditions. For this purpose he introduced the semplification that each body can be regarded as an elastic half-space loaded over a small elliptical region of its plane surface.

Hertz formulated four key assumptions:

- Small strain: within elastic limits
- Surfaces are continuous (smooth) and non-comforming
- The significant dimensions of the contact area must be small compared (a) with the dimionsions of each body and (b) with the relative radii of curvature of the surfaces.
- The surfaces are frictionless

Under these assumptions, Hertz derived equations describing the local behavior of contacting bodies. The following formulas are valid only for circular contact, i.e., between two spheres or between a sphere and a flat surface.

	Circular contact
Radii of relative curvature	$\frac{1}{R_x} = \frac{1}{R_{x1}} + \frac{1}{R_{x2}} \& \frac{1}{R_y} = \frac{1}{R_{y1}} + \frac{1}{R_{y2}}$
Contact modulus	$E^* = (\frac{1-\nu_1^2}{E_1} + \frac{1-\nu_2^2}{E_2})^{-1}$
Load	P
Contact radius	$a = \left(\frac{3}{4}\frac{PR}{E^*}\right)^{\frac{1}{3}}$
Maximum contact pressure	$p_0 = \frac{1}{\pi}\left(\frac{6P(E^*)^2}{R^2}\right)^{\frac{1}{3}}$
Contact pressure	$p(x,y) = p_0\left(1 - \frac{x^2}{a^2} - \frac{y^2}{a^2}\right)^{\frac{1}{2}}$
Interpenetration	$\delta = \frac{a^2}{R} = \frac{1}{2}\left(\frac{9P^2}{2(E^*)^2R}\right)^{\frac{1}{3}} \sim P^{\frac{2}{3}}$

Table 2.1: Hertz formulae for circular contact

It is important to clarify that δ represents the interpenetration, i.e., the relative displacement along the z-axis of the two reference frames of the undeformed solids. In many cases, an approximation is used in which the interpenetration is estimated from the displacement of the centers of mass of the bodies. From Table 2.1, it is evident that the relationship between δ and the applied load P is nonlinear. This relationship can be expressed as

$$P = A_j\,\delta^{3/2}, \tag{2.1}$$

where A_j depends only on the geometries and material properties of the two bodies.

This nonlinear dependence between the load and the displacement governs the propagation of solitary waves (SWs) in granular chains.

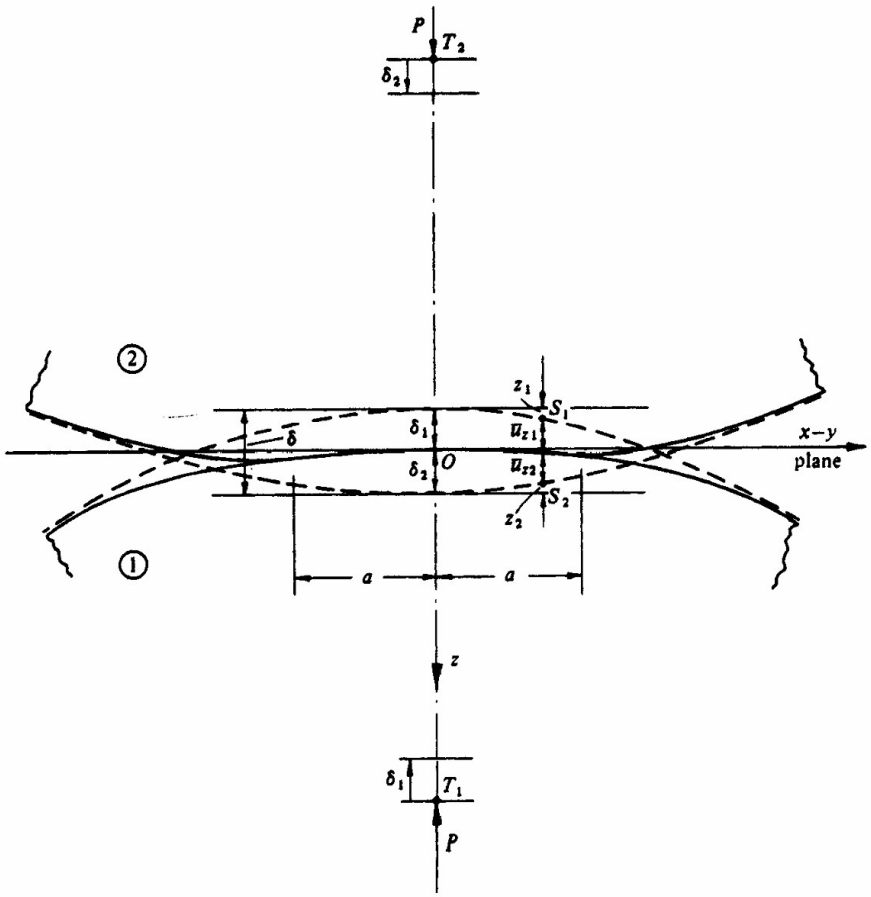

Figure 2.5: Mutual approach between two bodies under the application of a load P. Taken from [2]

In Contact Mechanics [2], Johnson defined the displacement field of each body both inside and outside the contact area. Inside the contact area:

$$u_z(r) = \frac{1-\nu^2}{E}\frac{\pi p_0}{4a}(2a^2 - r^2), \qquad r \leq a \tag{2.2}$$

$$u_z(r) = \frac{1-\nu^2}{E}\frac{p_0}{2a}\left[(2a^2 - r^2)\sin^{-1}\left(\frac{a}{r}\right) + r^2\frac{a}{r}\left(1 - \frac{a^2}{r^2}\right)^{1/2}\right], \qquad r \geq a \tag{2.3}$$

It is important to be aware of the limitations of Hertz's theory. First, it is valid only for frictionless surfaces, whereas real contacts always involve some friction. Moreover, the theory is formulated for static conditions only; dynamic effects, such as damping, are not considered in Hertz's original formulation.

2.2 Solitary Waves

After understanding the origin of the nonlinearity, it is important to identify the parameters that characterize solitary waves (SWs) and the factors that influence their propagation.

2.2.1 Parameters for the characterization of the Solitary waves

We now consider a one-dimensional granular chain composed of spherical beads of identical size and material, aligned along a single direction. A classical example of such a system is Newton's cradle, shown in Fig. 2.1. A schematic representation of a granular crystal chain used for non-destructive evaluation is reported in Fig. 2.6.

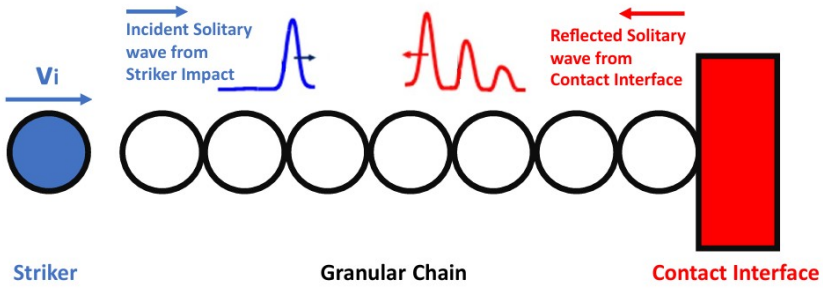

Figure 2.6: 1D granular chain for Non Destructive Evaluation

The mutual interactions between adjacent beads can be described using Hertz's contact law. Under this assumption, the equation of motion for the i-th bead is:

$$m_i \ddot{x} i = A_i (x_{i-1} - x_i)_+^{\frac{3}{2}} - A_{i+1}(x_i - x_{i+1})_+^{\frac{3}{2}}, \tag{2.4}$$

where A_i denotes the contact stiffness coefficient between beads $i-1$ and i, and the operator $(s)_+$ is defined as $(s)_+ = s$ for $s > 0$ and $(s)_+ = 0$ for $s \leq 0$.
As discussed in the previous section, the propagation of solitary waves in granular chains is strongly influenced by scattering phenomena occurring at interfaces between adjacent beads. In their theoretical analysis, V.F. Nesterenko et al. [5] showed that the energy carried by a highly nonlinear solitary wave has a compact spatial support. In chains composed of spherical elements, the wave is typically confined within a wavelength of approximately five particles.
To better understand the energy exchange mechanisms during SW propagation, let us consider the configuration shown in Fig. 2.6. Initially, the granular chain is at

rest. At time $t = 0$, a striker impacts the first bead of the chain, generating a solitary wave. The energy evolution of the system can be described as follows:

- At $t = 0$, the striker impacts the chain. The total energy of the system is given by the kinetic energy of the striker.
- At a time t >0 the beads start moving along the direction of the chain. The total energy is given by the sum of the kinetic energy of each bead and the elastic potential energy stored at the contacts.
- At a time t= t_t, the SW reaches the last sphere, which begins to penetrate the wall. When the maximum penetration is reached, the total energy is mainly given by the elastic potential energy at the contact between the last bead and the wall (kinetic energy is not zero, since some spheres in the chain are still in motion).
- After this point, the loading cycle is completed and the unloading cycle begins. The unloading cycle propagates back in the chain in the form of a reflected solitary wave.

The kinetic and potential energy contributions can be defined as:

- Kinetic energy of the i-th bead: $K_i = \frac{1}{2} m_i v_i^2$
- Elastic potential energy stored at the i-th contact: $U_i = \frac{2}{5} A_i (x_{i-1} - x_i)^{\frac{5}{2}}$

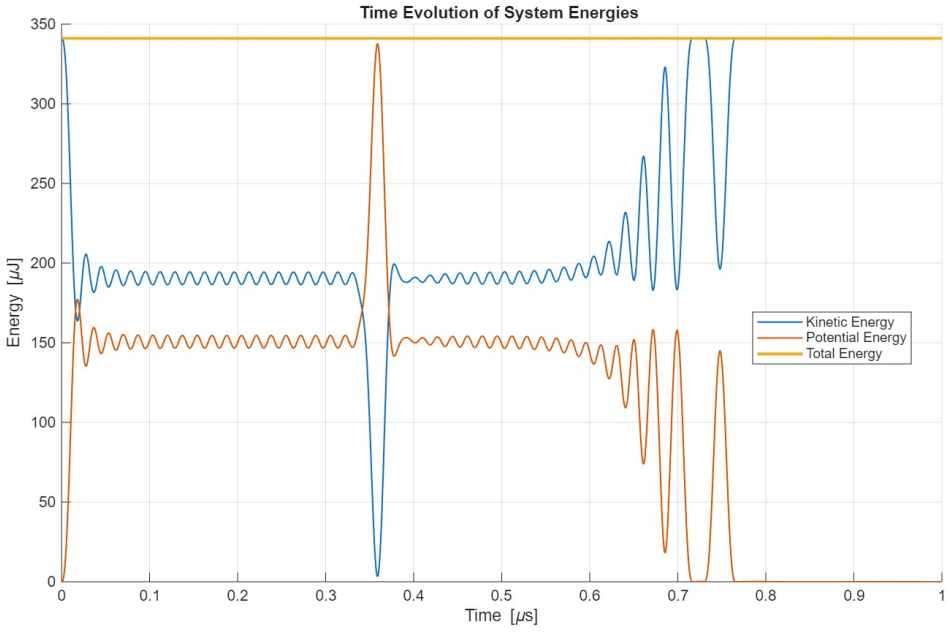

Figure 2.7: Time evolution of system energies

In this first analysis, the collision process is assumed to be fully elastic. By equating the kinetic energy of the striker to the total energy carried by the solitary wave at the wall, it is possible to derive an expression for the contact time T_c between the last bead and the wall [3]:

$$T_c = \tau_c m^{\frac{2}{5}} V_s^{-\frac{1}{5}} A_w^{-\frac{2}{5}} \tag{2.5}$$

where m is the bead mass, V_s is the striker velocity, A_w is the contact stiffness coefficient between the last bead and the wall and τ_c is a dimensionless contact time.
This equation highlights the dependence of the contact time on the mechanical properties of the wall through A_w. Moreover, it shows that increasing the striker velocity results in a decreasing of the contact time.
We can now define the traveling time T_t, i.e. the time required for the incident solitary wave and the reflected solitary wave to propagate along the chain:

$$T_t = \frac{2NR}{V_{inc}} + \frac{2NR}{V_{ref}} \tag{2.6}$$

where N is the number of beads, R is the bead radius, and V_{inc} and V_{ref} denote the velocities of the incident and reflected solitary waves, respectively.

The time of flight (TOF) of the waves can then be expressed as

$$TOF = T_c + T_t \tag{2.7}$$

If dissipation effects are neglected $V_{inc} = V_{ref}$. This assumption represents a strong approximation, since in real granular crystals a certain amount of energy dissipation is always present. To account for dissipative effects, Falcon *et al.* [6] introduced the coefficient of restitution ϵ. For a collision between a chain of beads and a plane at rest, the coefficient of restitution ϵ can be expressed as [7]:

$$\epsilon_n = \frac{\sum_{i=1}^{N} v_i^f}{\sum_{i=1}^{N} v_i^i} \tag{2.8}$$

where v_i^f and v_i^i denotes the velocity of the i-th bead respectively after and before the collision.
According to Yang et al. [8], the coefficient of restitution can be used to define the amplitude ratio of the reflected wave (ARR) as

$$ARR = \left(\frac{v_{ref}}{v_{inc}}\right)^{\frac{6}{5}} = \epsilon^{\frac{6}{5}} \tag{2.9}$$

This relation links the dissipative properties of the bead–wall interaction to the amplitude of the reflected solitary wave. Since the time of flight (TOF) also depends on the velocity of the reflected solitary wave, there is a correlation between these two parameters.

As a consequence, a faster v_{ref} results in both a higher ARR and a shorter time of flight (TOF), whereas increasing dissipation leads to a reduced reflected amplitude and a longer TOF.
Therefore, TOF and ARR are strongly correlated and physically meaningful parameters. They play a key role in the analysis presented in the later chapters and are fundamental for characterizing the system response in the design of the evaluation tool.

2.2.2 Influences on the solitary waves

Now that the most important paramaters for the characterization of the SWs have been clearly defined, understanding the main features that influence these parameters becomes crucial for achieving the final goal of designing a non-destructive evaluation tool.

Effect of Young's modulus

In [3], Yang et al. investigated the interaction between a granular chain and elastic media with different Young's moduli. For this purpose, they compared the response of a hard elastic medium, such as stainless steel, with that of a soft elastic medium, such as PTFE. Their experiments showed that the displacement profiles of the spheres differ significantly depending on the characteristics of the adjacent medium.
These differences in behavior arise from the fact that, during the penetration process into a soft wall, the last sphere may detach from the adjacent sphere in the chain. This phenomenon can lead to two main consequences:

1. A significant increase in the delay time before the last sphere rebounds under the resistance of the elastic medium.

2. A second impact between the last sphere and the rest of the chain due to the wall elasticity. When this occurs, the second encounter triggers the formation of a secondary solitary wave (SSW).

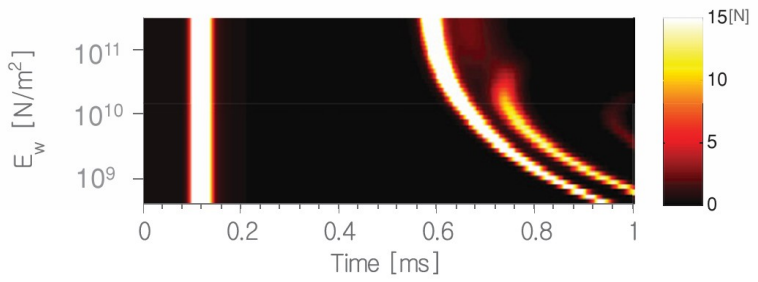

Figure 2.8: Influence of Young's modulus of the wall on T_c and the generations of SSW [3].

Hence, there exists a critical value of Young's modulus above which secondary solitary waves (SSWs) are generated. This value corresponds to the condition in which the displacement between the last sphere and the wall is equal to the displacement between the second-to-last sphere and the last sphere.

Thickness of the wall

To understand how the wall thickness affect the response of the granular system, it is necessary to analyze the dynamics of the collision between the last sphere in the chain and the wall.
When the last bead in the chain collides with the wall, under the one-dimensional approximation and neglecting surface and flexural waves in the medium [3], a longitudinal wave propagates along the axial direction of the wall at velocity c, i.e., the speed of sound in the material (for stainless steel, $c \approx 5000\,\mathrm{m/s}$).

The wave reflects at the opposite face of the wall and propagates back toward the contact interface. During the contact time T_c between the last sphere and the wall, the longitudinal wave travels a distance equal to cT_c. Two different cases may arise:

1. $L \leq \frac{cT_c}{2}$: the energy initially transferred to the wall is partially returned to the granular chain due to the reflection of the wave. In this case, the energy loss is minimal.

2. $L > cT_c$: the longitudinal wave does not return to the contact region within the time T_c, and part of the total energy is dissipated within the wall. The amount of energy dispersed due to this mechanism is approximately 5%.

Here, L denotes the thickness of the elastic medium. This energy loss results in a decrease of the ARR of the solitary waves.
However, decreasing the wall thickness below a certain value (plate) can lead to an

increase in the inelastic effects of the wall. This corresponds to the case in which the diameter D of the spheres in the chain becomes comparable to the plate thickness t. In this situation, the impact between the last bead and the wall is no longer comparable to that between a sphere and a half-space, and part of the energy is transmitted to the wall, which starts vibrating. As a result, the reduction of the plate thickness contributes to an elongation of the contact time T_c and to a reduction of the amplitude reflected ratio ARR. In [8], Yang et al. found that for a ratio of $D/t \approx 5$, the reflected solitary wave becomes negligible and the energy is almost entirely transmitted to the plate.

Effect of the boundary conditions

The interaction between the granular chain and a thin plate strongly depends on the position of the contact point relative to the plate's boundary conditions. In particular, reflected waves exhibit a high ARR when the impact occurs close to the boundaries. As the impact point moves further away, dissipative effects increase and the ARR decreases. This phenomenon arises from a local strengthening effect induced by the boundary conditions, which constrain the dynamic response of the plate.

However, beyond a certain distance from the boundaries, Young et al. [8] demonstrated that the ARR becomes approximately constant, defining a critical distance beyond which the reflected solitary waves are essentially insensitive to boundary effects.

It is important to note that the influence of boundary conditions is not limited to thin plates but also applies to walls of any geometry. However, the critical distance strongly depends on the thickness of the linear elastic medium. For thicker walls, the critical distance becomes so small that boundary effects can usually be neglected in the evaluation of reflected solitary waves.

Effect of the mass of the spheres in the chain

From Eq. 2.5, the relation between the contact time T_c and the mass m of a sphere is defined for the case of the last sphere impacting the wall. However, Hertz theory allows one to relate the sphere-to-sphere interaction to the sphere-to-wall interaction (more precisely, the interaction with an elastic half-space). Therefore, changing the mass of the spheres in the entire chain affects not only the contact between the last sphere and the wall but also all interactions within the chain, and consequently the propagation of solitary waves (SWs).

In particular, the relation between the contact time and the sphere mass is strongly nonlinear, due to the exponent $\frac{2}{5}$:

$$T_c \sim m^{\frac{2}{5}} \tag{2.10}$$

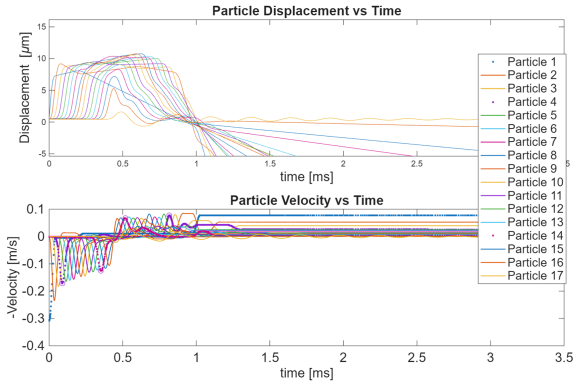

(a) $m_s = 0.013$ Kg

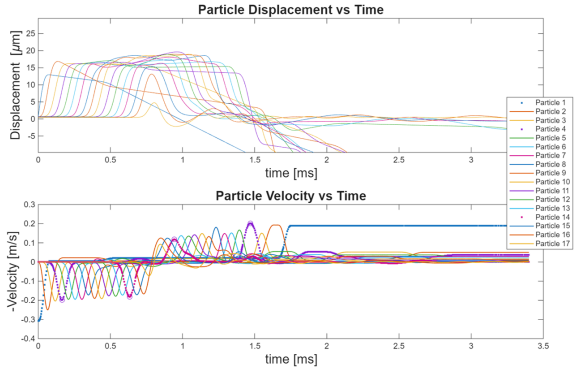

(b) $m_s = 0.07$ Kg

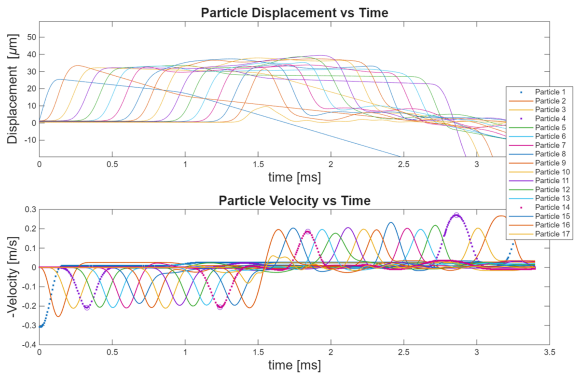

(c) $m_s = 0.5$ Kg

Figure 2.9: Effect of the mass of the spheres on the SWs

From Fig. 2.9, it is evident that the smaller the mass of the spheres in the

chain, the shorter the contact time at each collision, and consequently, the faster the propagation of the solitary waves. In Section 2.2.1, it is discussed that reducing the contact time would, in principle, lead to an increase in the amplitude of the wave peaks and, thus, in the amplitude reflected ratio (ARR). However, in Fig. 2.9(a) shows that a smaller-mass impacting sphere results in lower initial kinetic energy. Although this causes the solitary wave to propagate faster due to reduced contact time, the lower energy reduces the wave peaks, leaving the ARR approximately unchanged. The same reasoning applies to spheres of different masses: variations in mass alter the wave speed and peak amplitude, but the ARR remains unaffected.

Chapter 3

Reference Experimental Framework

In this chapter, the experimental setup and testing procedure of the test rig located at the University of Illinois at Urbana-Champaign are presented. It should be noted that the experimental activity itself is not part of the present work, and the author was not involved in the design or execution of the experiments.

However, the experimental results obtained from this test rig provide the reference data used to validate the numerical model developed in this study. For this reason, the experimental setup and testing procedure are briefly described in the following sections.

The setup is designed to investigate the application of solitary waves (SWs) to contact analysis and allows the study of the frictional state at the contact interface. In the present work, however, the analysis is limited to the frictionless case.

Understanding the experimental setup and testing procedure is therefore important, as they define the physical system that the numerical model aims to reproduce.

3.1 Experimental setup

In this section, the experimental setup for the study of SWs is described. The components of the experimental setup can be summarize as follow:

- (1) Granular chain
- (2) Steel assembly
- (3) Leaf springs
- (4) Static pulling load

- (5) Shaker
- (6) Lasers

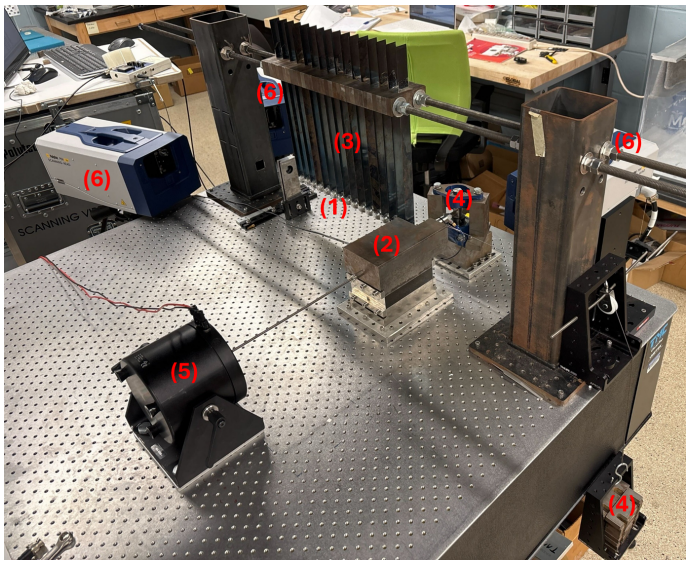

(a)

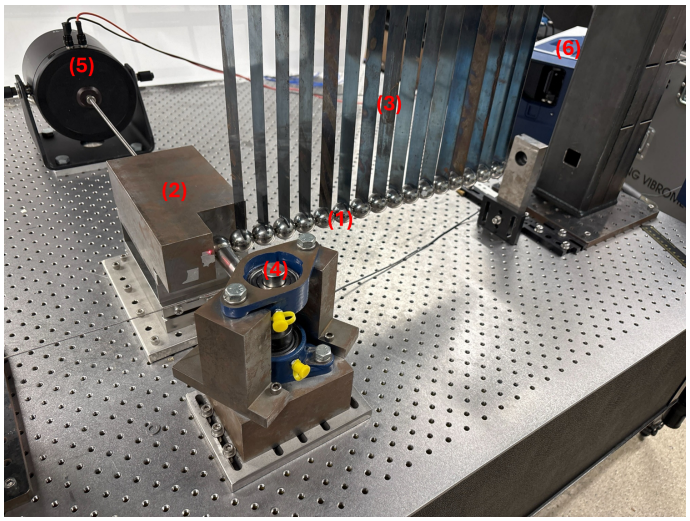

(b)

Figure 3.1: University of Urbana Illinois Experimental setup

Granular Chain

The granular chain in this setup is composed of 17 steel spheres aligned along a single direction. As explained in the previous section, this component enables the generation and propagation of the SWs.

Steel Assembly

This assembly is placed at the end of the granular chain, and its dynamics affect the RSWs. It is composed of the following elements and will be the subject of a detailed analysis in a subsequent section.

- Block
- Sheets
- Sheets Support
- Support
- Plate

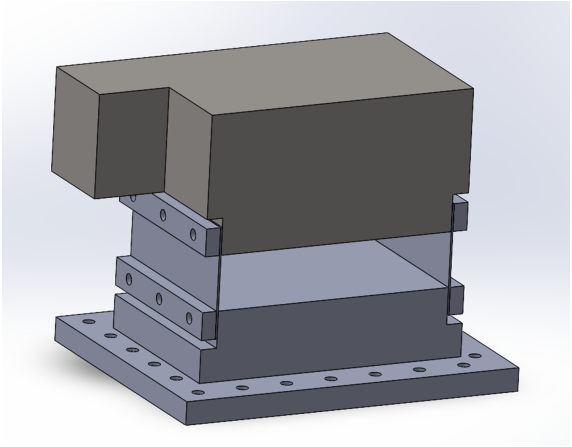

Figure 3.2: University of Urbana Illinois CAD Assembly

Leaf Springs

The leaf springs are thin steel strips clamped to the first 16 of the 17 spheres in the chain. They serve two main purposes:

1. Structural support: they sustain the spheres while constraining motion to the chain direction, preventing displacement along other degrees of freedom.
2. Preloading: they apply a controlled precompression to the spheres, ensuring consistent initial conditions for test repeatability.

Pulling Arm

The pulling arm is clamped to the last sphere of the chain and serves to support it while applying a static normal load that pulls the sphere toward the assembly. The role of this component is similar to that of leaf springs, although it also provides an additional function. Specifically, the pulling arm ensures the presence of a normal load, allowing friction to develop between the last sphere and the assembly.

Shaker

The shaker is connected to the back of the moving block and, in experiments where friction is required, excites the block at a frequency of 100 Hz in order to generate relative motion between the assembly and the last sphere of the chain. This component is not considered in the present work, since the analysis is limited to the frictionless case.

Lasers

Three high-precision lasers are directed at different spheres in the chain in order to monitor their displacement and velocity.

Now that the experimental setup has been presented, it is possible to describe how the experiment works.

3.2 Experiment Process

At the initial condition, 16 of the 17 spheres in the chain rest in equilibrium, while the first sphere is released with a controlled velocity along the direction of the chain. When the first sphere impacts the second sphere, an incident solitary wave is generated and starts propagating through the chain as a sequence of subsequent impacts between spheres.

When the solitary wave reaches the end of the chain, part of its energy is transmitted to the assembly, while most of it is reflected in the form of reflected solitary waves that propagate back through the chain. From this moment on, the last sphere experiences subsequent impacts with the wall due to the static pulling load applied to it and the wall dynamics, generating several reflected solitary waves (RSWs) that propagate through the chain.

The entire process occurs within a total time of approximately 3 ms, and the displacements of the spheres in the chain are on the order of a few micrometers.

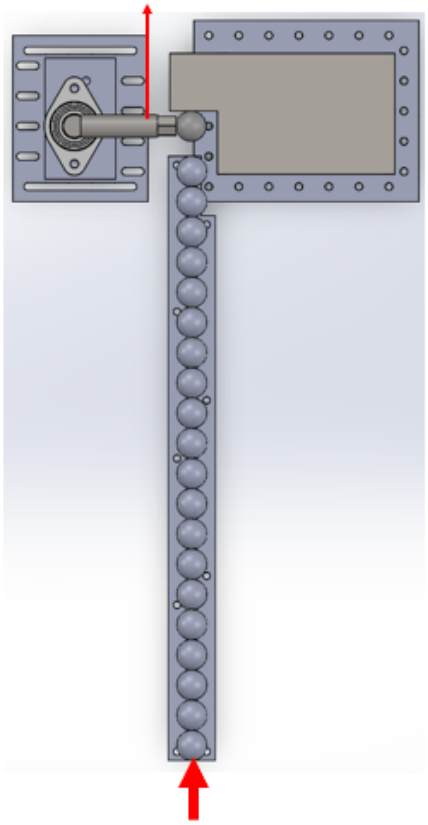

Figure 3.3: CAD Experimental Process at the University of Illinois at Urbana–Champaign

Chapter 4

Numerical Modelling: Discrete Element Method

In this chapter, the numerical method used to model the propagation of SWs in the granular chain is presented. This numerical model for the granular chain is implemented in an existing MATLAB code developed at Imperial College and serves as the starting point for the analysis presented in this thesis.

4.1 Numerical Model for Granular Crystals

The numerical modeling of the granular chain is performed using the Discrete Element Method (DEM). This approach is particularly suitable for systems composed of discrete bodies interacting through localized contact forces.

In DEM, each particle of the granular chain is treated as an individual rigid body with its own mass and degrees of freedom. The motion of each particle is governed by Newton's second law, while the interaction between particles is described by nonlinear contact laws.

The numerical model is based on the well-known Hertz contact law. For completeness, Eq. 2.4 is reported:

$$m_i\ddot{x}_i = A_i(x_{i-1} - x_i)_+^{\frac{3}{2}} - A_{i+1}(x_i - x_{i+1})_+^{\frac{3}{2}}, \tag{4.1}$$

and defining:

$$\delta_i = [x_{i-1} - x_i]_+, \qquad i \in \{1, ..., N\}.$$

However, Hertz theory is derived under the assumptions discussed in Chapter 2 and is strictly valid for static contact conditions. Since solitary waves are dynamic phenomena, the pure Hertz model alone is not sufficient to accurately describe the

interactions along the granular chain.

For this reason, additional terms accounting for dynamic effects at the contacts, which manifest as dissipation, are introduced: [9] [3]

$$m_i\ddot{x}_i \;=\; (A_i\delta_{(i)+}^{\frac{3}{2}} - A_{i+1}\delta_{(i+1)+}^{\frac{3}{2}}) \;+\; (\gamma_i\dot{\delta}_i - \gamma_{i+1}\dot{\delta}_{i+1}) \tag{4.2}$$

$$i \in \{1, 2, ..., N\}$$

where the parameters A_i represent the Hertzian contact stiffness and are defined as:

$$A_i = \begin{cases} A|_c = \dfrac{E\sqrt{2R}}{3(1-\nu_s^2)} & \text{if } i \in \{1, ..., N\} \\ A|_w = \dfrac{4\sqrt{R}}{3}\left(\dfrac{1-\nu_s^2}{E_s} + \dfrac{1-\nu_w^2}{E_w}\right)^{-1} & \text{if } i = N+1 \end{cases}$$

Similarly, the dissipation coefficients are defined as:

$$\gamma_i = \begin{cases} \gamma|_c & \text{if } i \in \{1, ..., N\} \\ \gamma|_w & \text{if } i = N+1 \end{cases}$$

Before proceeding, it is important to clarify the meaning of the index range $i \in \{1, ..., N+1\}$. Each equation describes the motion of the i-th sphere and depends on the deformation of the adjacent contact interfaces i and $i+1$.

The system of equations 4.2 describes the dynamics of the contacts between the spheres in the chain. However, for the purposes of the present work, it is necessary to introduce an additional term accounting for the presence of the leaf springs. For this purpose, each leaf spring is modeled as a linear spring with stiffness k_{leaf}, connected on one side to a sphere and on the other side to the ground. The corresponding force term is therefore added to all equations in the range $i \in \{1, ..., N\}$, whereas the equation associated with the last contact will be slightly different.

$$m_i\ddot{x}_i \;=\; (A_i\delta_{(i)+}^{\frac{3}{2}} - A_{i+1}\delta_{(i+1)+}^{\frac{3}{2}}) \;+\; (\gamma_i\dot{\delta}_i - \gamma_{i+1}\dot{\delta}_{i+1}) \;-\; k_{leaf}(x_i - x_{leaf}) \tag{4.3}$$

$$i \in \{1, 2, ..., N\}$$

For the last contact, i.e. the contact interface between the last sphere in the chain and the surface of the assembly, two additional contributions must be considered:

$$m_i\ddot{x}_i = (A_i\delta_{(i)+}^{\frac{3}{2}} - A_{i+1}\delta_{(i+1)+}^{\frac{3}{2}}) + (\gamma_i\dot{\delta}_i - \gamma_{i+1}\dot{\delta}_{i+1}) + F_{preload} - F_{wall} \tag{4.4}$$

$$i = N + 1$$

While the preload is known, the term associated with the wall will be investigated in the later section.

4.2 Numerical Model for the Wall

Experimental observations show that the wall dynamics strongly affect the RSWs and so it is very important to define a consistent numerical model of the wall. However, identifying a model that accurately reproduces the dynamics of the actual wall is very challenging.

For this purpose, three different approaches have been implemented.

4.2.1 Ideal Half Space

In this first approach, the wall is modeled as an ideal half-space, meaning it is treated as a semi-infinite elastic medium that can deform locally under the interaction with the last sphere of the chain. In the present work, however, the wall is modeled as infinitely rigid, and all deformation is assumed to occur at the sphere level.

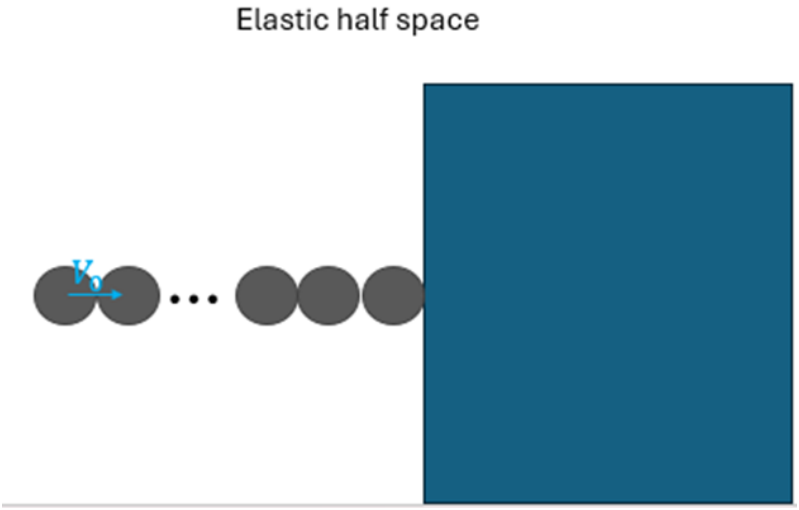

Figure 4.1: Elastic Half Space

4.2.2 Single Degree of Freedom Wall

In this second approach, the wall is modeled as a mass connected to the ground through a linear stiffness. In this way, the wall can oscillate and its dynamics are governed by the mass and stiffness values. These parameters can be tuned in order to reproduce different natural frequencies of the wall.

If the wall is modeled as a single-degree-of-freedom system, the wall-dependent term in Eq. 4.4 becomes:

$$f_{wall} = k_{wall} x_{wall} + c_{wall} \dot{x}_{wall} \tag{4.5}$$

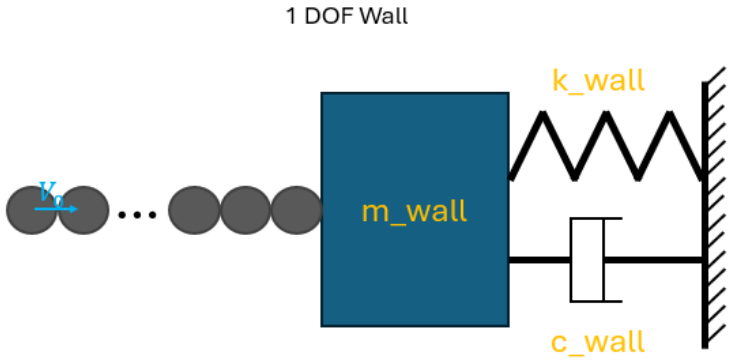

Figure 4.2: Single-degree-of-freedom model of the wall

4.2.3 Reduced Order Model Wall

This third approach is the most complex among the proposed approaches, but it is also the most consistent with the actual dynamics of the assembly.

This method consists of performing a frequency analysis of the assembly in Abaqus in order to extract its modal shapes. A reduced order model (ROM) is then used to generate the mass and stiffness matrices only for the region of interest.

The frequency analysis of the assembly and the coupling between the MATLAB code and the ROM will be the subject of the next chapter.

Chapter 5

Finite Element Analysis and Model Reduction

During the experimental tests, a hammer test was performed in order to extract the modal properties of the assembly. This test result is very important as a reference for the numerical model of the assembly.

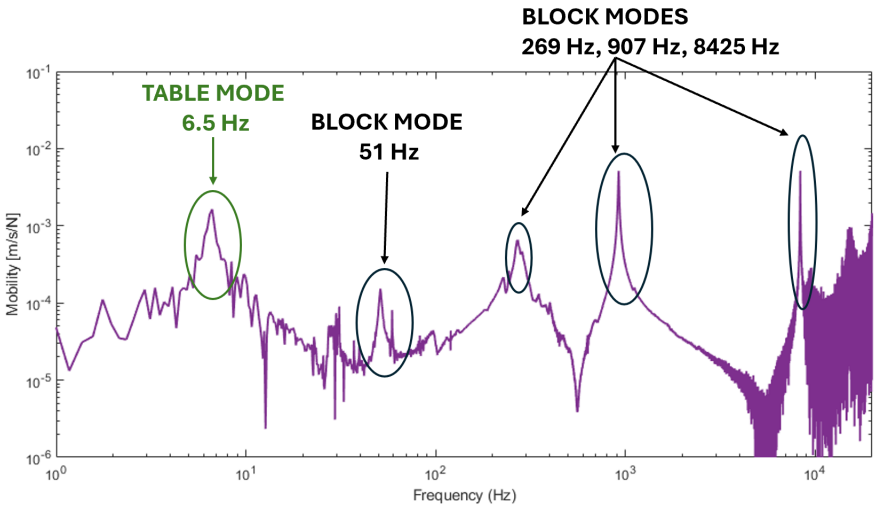

Figure 5.1: Modal forms of the assembly

In Fig. 5.1, the Fast Fourier Transform (FFT) of the assembly response is shown, where each peak corresponds to a modal form. From a preliminary analysis, the first peak at a frequency of 6.5 Hz can be neglected. This peak is not associated with a mode of the assembly, but rather with a vibration mode of the table on which the assembly is placed. Therefore, it is not considered in the present analysis of the collision with the granular chain.

The experimental modal frequencies of the assembly can be summarized in the

following table:

	1st mode [Hz]	2nd mode [Hz]	3rd mode [Hz]	4th mode [Hz]
Experimental	51	269	907	8425

Table 5.1: Natural frequencies of the assembly

5.1 Mesh convergency analysis

Now that the desired behavior of the assembly is well known, a numerical model of the assembly was implemented in Abaqus. However, the definition of the boundary conditions and the modeling of the connections between components, such as bolted joints, are challenging. In particular, several assumptions can be made regarding the constraints and the stiffness of the bolted interfaces.

For this reason, different modeling configurations were tested in order to identify the setup that best reproduces the experimental dynamic behavior of the assembly.

First, a mesh convergence analysis was performed. In particular, the components that most affect the results are the sheets, since they have the lowest stiffness in the entire assembly. For the mesh convergence analysis, two different configurations of constraints between the components were compared:

- Full tie constraint
- Screw tie constraint (the tie constraint is applied only in the regions where the screws are located)

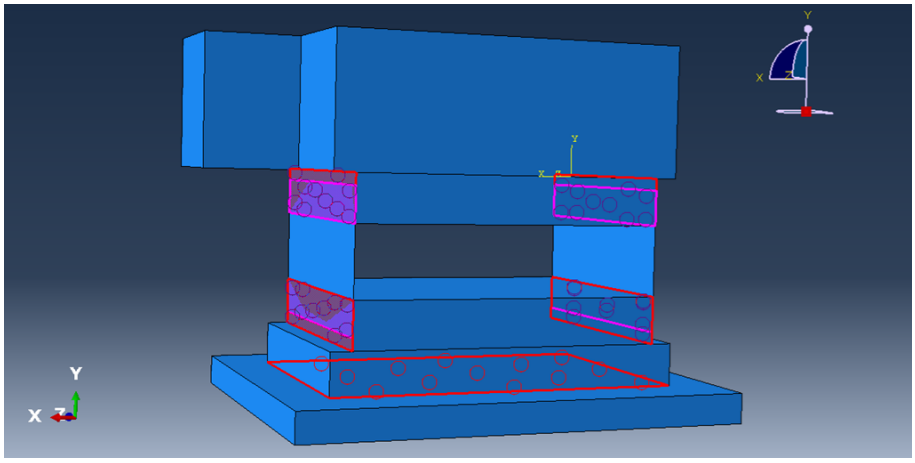

Figure 5.2: Full tie constraint assembly

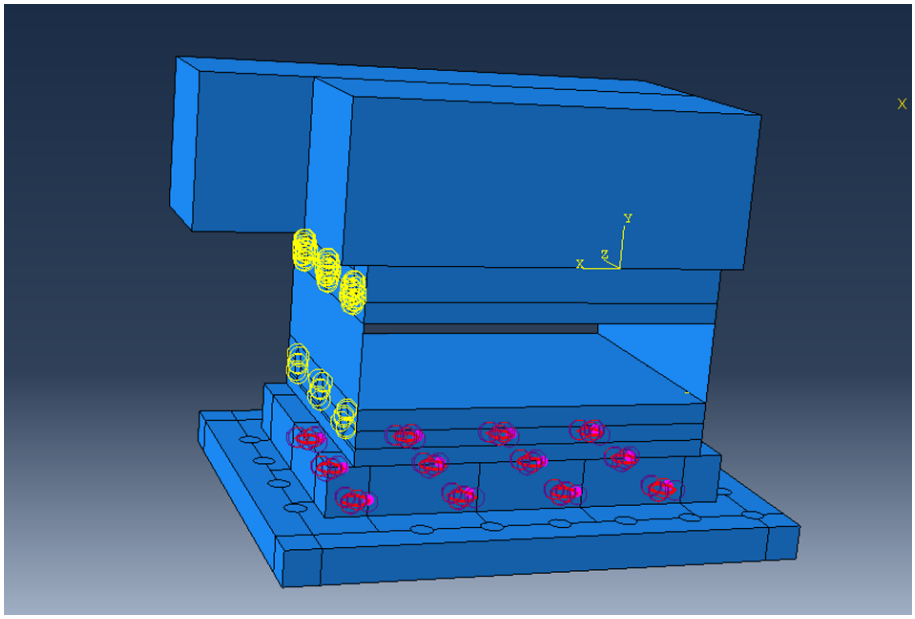

Figure 5.3: Screw tie constraint assembly

These two configurations represent the upper and lower bounds for the stiffness of the system.

In the mesh convergence analysis, different mesh sizes for the sheets were compared, with particular attention to the first mode shape, since it mainly depends on the dynamics of the sheets and on the connection between the sheets and the block.

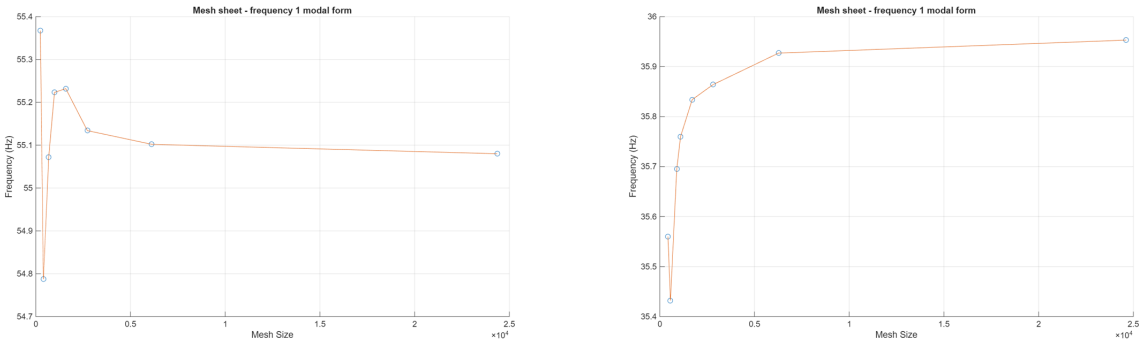

Full tie assembly Screw tie assembly

Figure 5.4: Mesh convergency analysis

In Fig. 5.4, it can be observed that the two plots show opposite trends as the mesh seed decreases.

For the full tie case, the smaller the mesh seed, the lower the frequency of the first mode shape. This occurs because, for coarse meshes, the full tie constraint limits the dynamics of the sheets even in regions where, in the actual assembly, the sheets are not constrained. As a result, refining the mesh leads to a reduction in the

effective stiffness.

On the other hand, in the screw tie constraint case, if the mesh seed is relatively large, the connection between the elements is poorly represented and the stiffness of the assembly is underestimated. However, increasing the number of elements in the mesh constrains more nodes of each component, leading to a more realistic representation of the structural behavior.

In both plots of Fig. 5.4, a numerical error appears for a mesh seed of 0.25 mm. This error arises because, in this analysis, the mesh seed of the sheets is the same as that of the block. Although the mesh sizes are equivalent, the different mesh patterns result in a local reduction of the overall stiffness.

The selected mesh seed for the sheets is 1.5 mm for both configurations, as it represents the best compromise between mesh convergence and computational time.

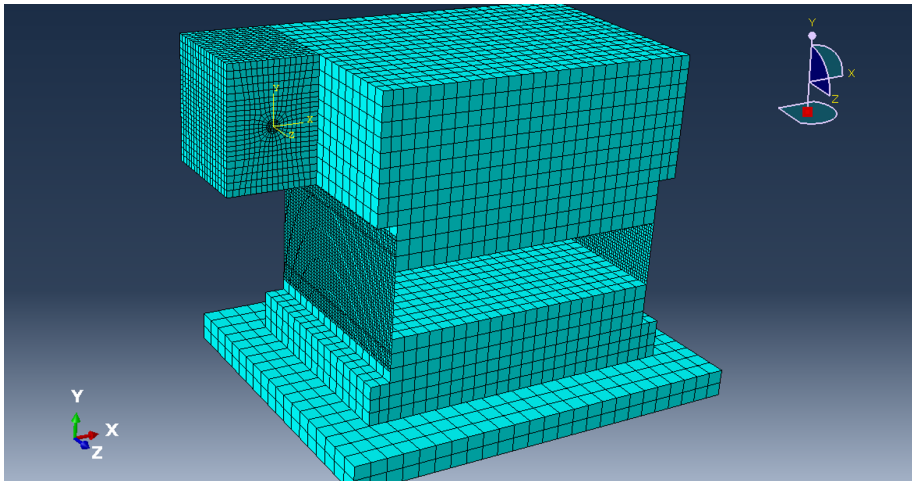

Figure 5.5: Mesh of the assembly

5.2 Abaqus Frequency analysis of the assembly

The next step consists of comparing the results obtained with the different constraint models in order to identify the configuration that best reproduces the actual dynamic behavior of the assembly.

For this purpose, a series of frequency analyses was performed for each constraint configuration. In these analyses, the model was built progressively by adding one component at a time in order to evaluate the contribution of each component to the modal behavior of the assembly.

The analysis started from the block constrained to the sheets. Subsequently, the support was added to the model, and finally the plate. This incremental approach makes it possible to clearly identify the influence of each component on the natural

frequencies and mode for of the system.

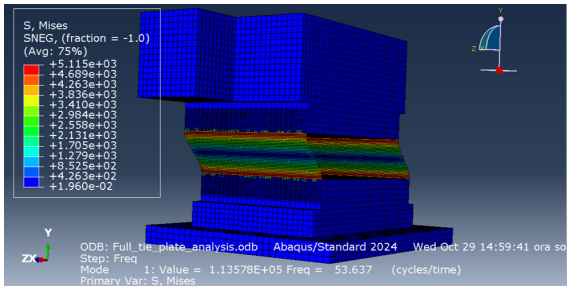

1st modal shape

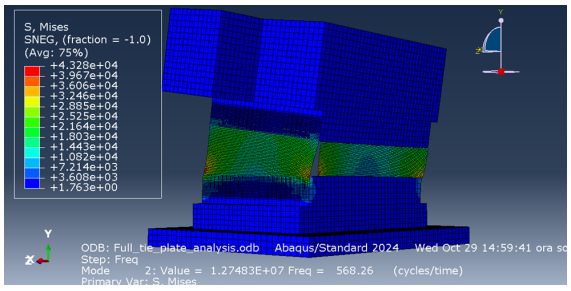

2nd modal shape

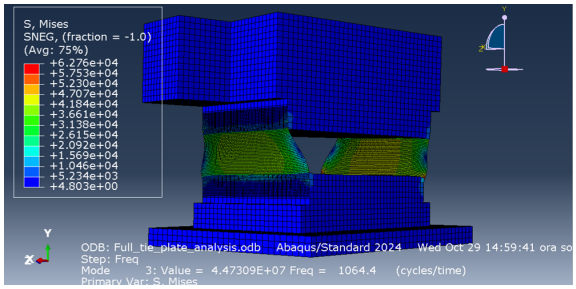

3rd modal shape

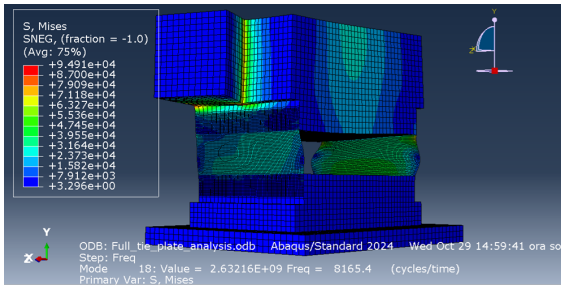

4th modal shape

Figure 5.6: Modal shapes of the assembly

The results from this analysis are summarized in the following table.

	1st mode [Hz]	2nd mode [Hz]	3rd mode [Hz]	4th mode [Hz]
Experimental	51	269	907	8425
Full tie	55.105	630	1134	8171.6
Full tie + Support	53.7	571	1069	8165
Full tie + Support + Plate	53.6	568	1064	8165
Screw tie	35.9	480.5	905	8140
Screw tie + Support	35	435	854	8136
Screw tie + Support + Plate	35	397	832	8147

Table 5.2: Comparison natural frequencies of the assembly

From the results in Tab. 5.2, several considerations can be drawn:

- The full tie constraint model accurately predicts the 1st mode, whereas the screw tie constraint model appears softer than the experimental data.
- Neither configuration properly describes the dynamics of the 2nd mode.

- Both configurations approximate the 3rd mode well, with higher accuracy achieved by the screw tie model.
- The 4th mode does not depend on the connection between the parts, since the results for the two configurations differ only slightly. In fact, Fig. 6.2 shows that the deformation associated with this mode occurs mainly at the block level.

The plot below illustrates the percentage impact of each component on the frequency of each mode:

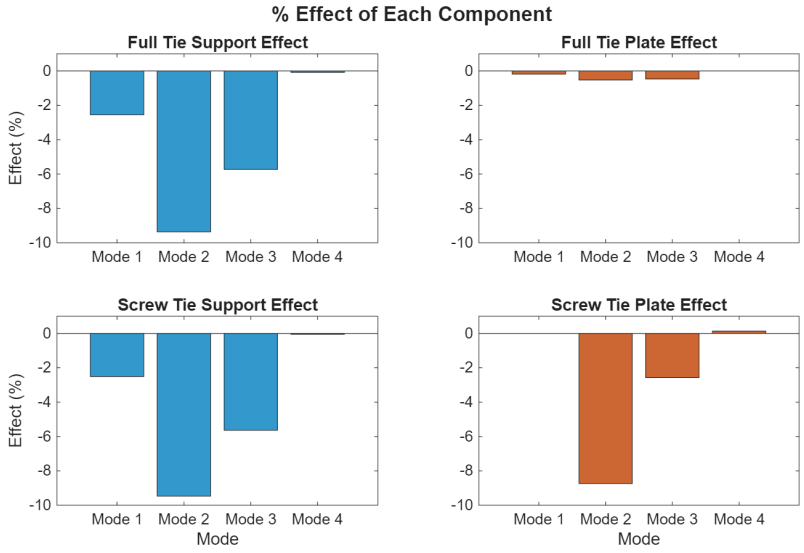

Figure 5.7: Percentage effect of each component

From Fig. 5.7, it is evident that the 4th mode is not influenced by the presence of the support or the plate. Therefore, for the full tie constraint, the role of the plate is negligible, as this component affects the result by less than 1%. However, the support has a similar influence on the results for both configurations.

Overall, both constraint configurations appear to be inadequate for accurately modeling the dynamic behavior of the assembly. Nevertheless, the results of this analysis provide useful insights into the physical behavior of the system.

In particular, the good agreement between the full tie model and the experimental data for the first mode suggests that the dynamic behavior of this modal shape is governed by a rigid connection between the sheets and the block in the direction of oscillation (Fig. 6.2).

However, the results for the second mode indicate that, in the tangential direction, the real assembly allows relative motion between the parts, which cannot be reproduced by the considered constraint models.

Finally, the third mode exhibits an intermediate behavior between the first and second modal shapes: the stiffness predicted by the full tie constraint is too high, whereas the screw tie model underestimates the stiffness of the system.

From the considerations above, the constraints between the parts were found to exhibit different stiffnesses in different directions. Therefore, the tie constraint proved to be unsuitable for accurately describing the dynamics of the actual assembly, and another constraint technique was implemented.

The coupling between the sheets and the block or support is now implemented by introducing reference points in each component, located at the centre of the screw holes. The reference points associated with the sheets are then connected to the corresponding reference points of the block or support through wire elements. The advantage of this technique is that the stiffness of the wire can be tuned independently in each direction.

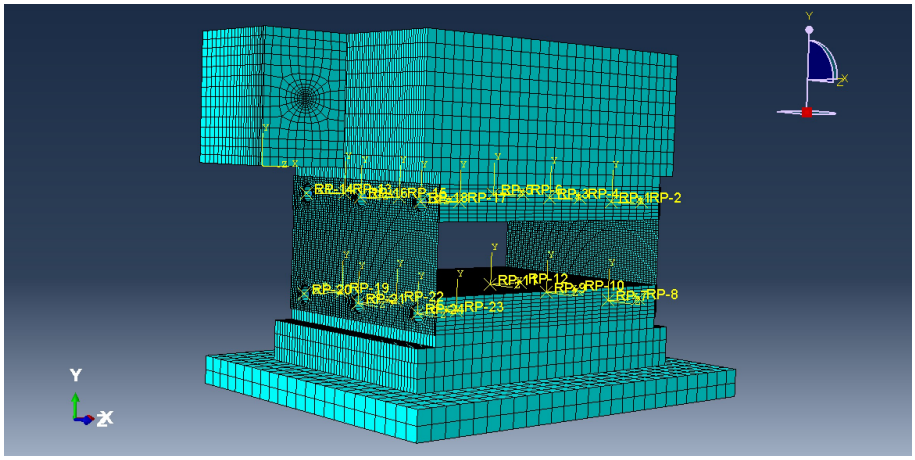

Figure 5.8: New connection between components

With this coupling technique, the dynamic behavior of the model also appears to be more representative of the actual assembly.

However, a critical issue of the current model is that the experimental second modal shape at 269 Hz and the experimental third modal shape at 907 Hz appear to be in conflict with each other. Increasing the tangential stiffness leads to a better match with the 907 Hz mode, at the expense of the agreement with the second modal shape at 269 Hz. On the other hand, matching the second experimental modal shape results in a deviation from the third modal shape at 907 Hz.

For this reason, two different numerical configurations were ultimately considered. In the first configuration the stiffness were tuned to match the 1st, 2nd, and 4th experimental modes, while in the second configuration were tuned to match the

1st, 3rd, and 4th experimental modes.

	1st mode [Hz]	2nd mode [Hz]	3rd mode [Hz]	4th mode [Hz]
Experimental	51	269	907	8425
Matching 2nd mode	50.9	273	709	8293
Matching 3rd mode	50.9	472	899	8286

Table 5.3: Frequency analysis results

The results obtained from these two modeling approaches will be compared and discussed in a subsequent section.

After identifying the most suitable constraint formulation for the components of the assembly, a Reduced Order Model (ROM) was implemented to enable the coupling between the Discrete Element Method (DEM), in MATLAB, and the Finite Element Method (FEM) model developed in Abaqus.

Chapter 6

Coupling DEM with FEM

Now that the numerical model for the granular chain (DEM) and the numerical model for the assembly (FEM) have been introduced, it is important to describe how these two models are coupled. For this purpose, a Reduced Order Model (ROM) has been implemented.

Applying a ROM to the full assembly model would be computationally prohibitive. Therefore, only the portion of the block where the impact with the last sphere of the granular chain occurs has been exported.

Although the implementation details of the ROM are not reported in this thesis, its role in the coupling strategy can be briefly outlined. The ROM is used to extract the mass and stiffness matrices only for the nodes of interest. Nevertheless, the dynamic behavior captured by these reduced matrices reflects the response of the entire assembly, as the ROM retains the influence of the surrounding structure while significantly reducing the computational cost.

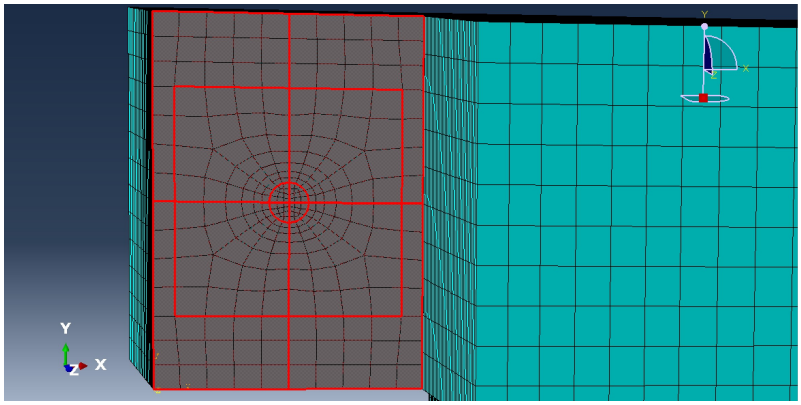

Figure 6.1: Recovery region

In Fig.6.1, the red region represents the nodes used for the ROM in order to generate the mass and stiffness matrices.

These two matrices, after being post-processed in Python, are exported to a .mat file and implemented in the wall-dependent term of Eq. 4.4.

6.1 Coupling Strategy

The critical point in the coupling between the ROM wall and the DEM method is the following:

When the solitary wave (SW) reaches the last sphere, the impact between the last sphere and the block occurs. In the real case, the sphere and the block are in contact over a small circular region. The radius of this contact area can be estimated using Hertzian contact theory and is approximately 300 μm. Although in a small area, the contact pressure is distributed.

On the other hand, during the coupling between the two methods, the impact between the two bodies occurs at a single mesh node rather than over a small contact area. Consequently, the contact force is no longer distributed but concentrated at a single point, which leads to an overestimation of the displacement at the contact node, generating a singularity. Moreover, the finer the mesh, the more pronounced the singularity at the contact point becomes.

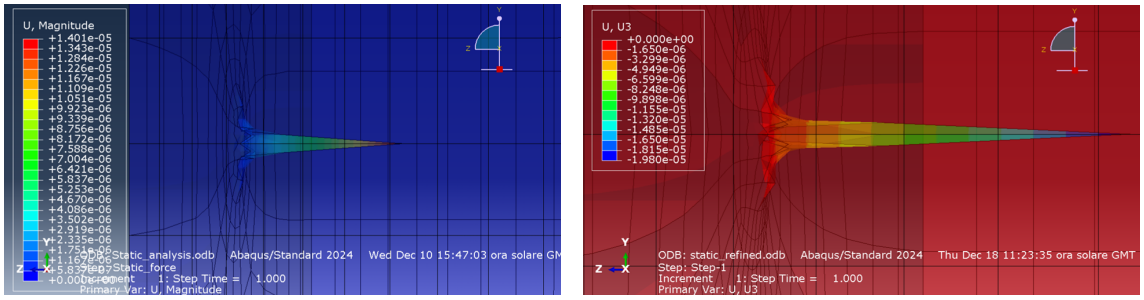

Coarse mesh Fine mesh

Figure 6.2: Effect of the mesh on the singularity

For this reason, using the contact node as a reference point for the wall dynamics would lead to an overestimation of the sphere displacement in the wall-normal direction, causing the system dynamics to deviate from the actual behavior due to the singularity at the contact point.

To avoid this issue, and considering that the focus of this analysis is not the local deformation of the wall but rather its global displacement field, the wall dynamics are recovered from the mean displacement of the two nodes surrounding the contact point. These nodes are hereafter referred to as recovery points, and their displacement is used in the calculation of the last sphere's interaction instead of the contact

point itself.

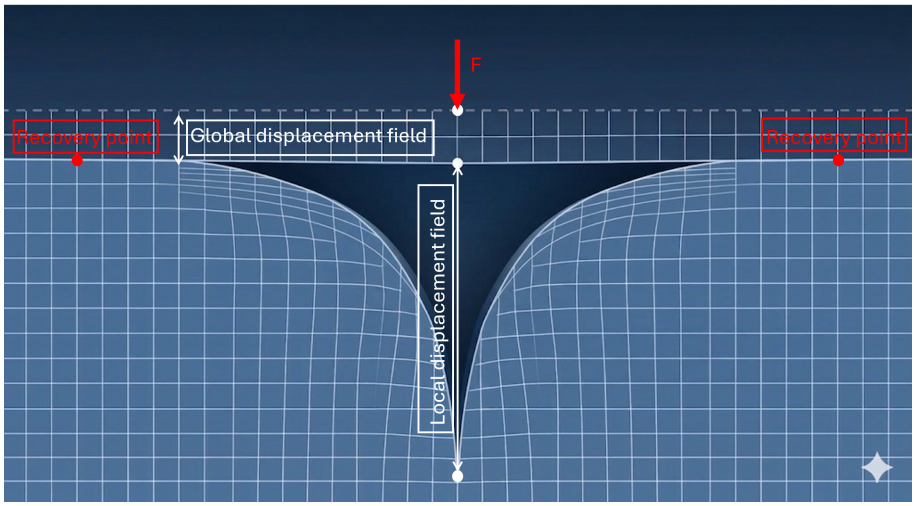

Figure 6.3: Solution adopted to mitigate the contact singularity

In Fig.6.3, the effect of the singularity on the local displacement field can be observed. To prevent this local behavior from influencing the coupling, the recovery points are selected as the nodes located farthest from the contact point, so that the wall motion used in the coupling reflects only the global dynamics.

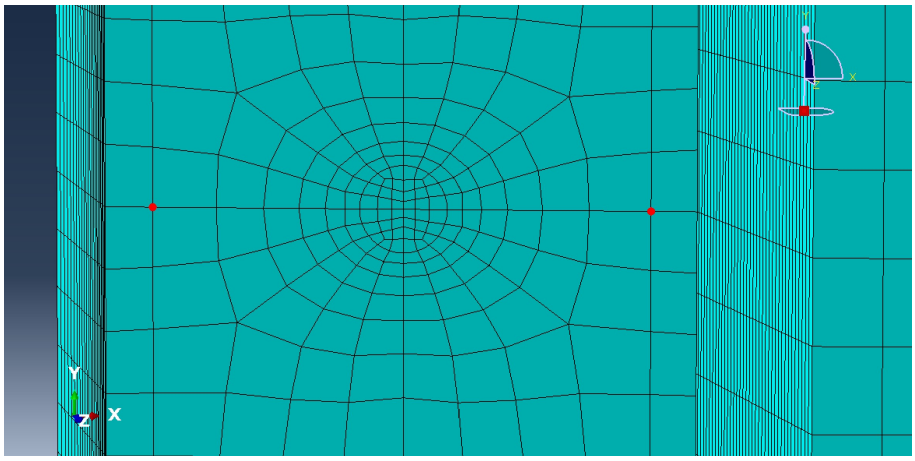

Figure 6.4: Location of the recovery points

6.2 Damping strategy

Now that the coupling strategy has been defined, the wall term can be incorporated into the equations of the granular chain. However, preliminary simulations revealed that no damping matrix had been defined for the wall. As a result, after the first impact the wall begins to oscillate, and subsequent impacts lead to an increase in both the amplitude and the frequency of these oscillations.

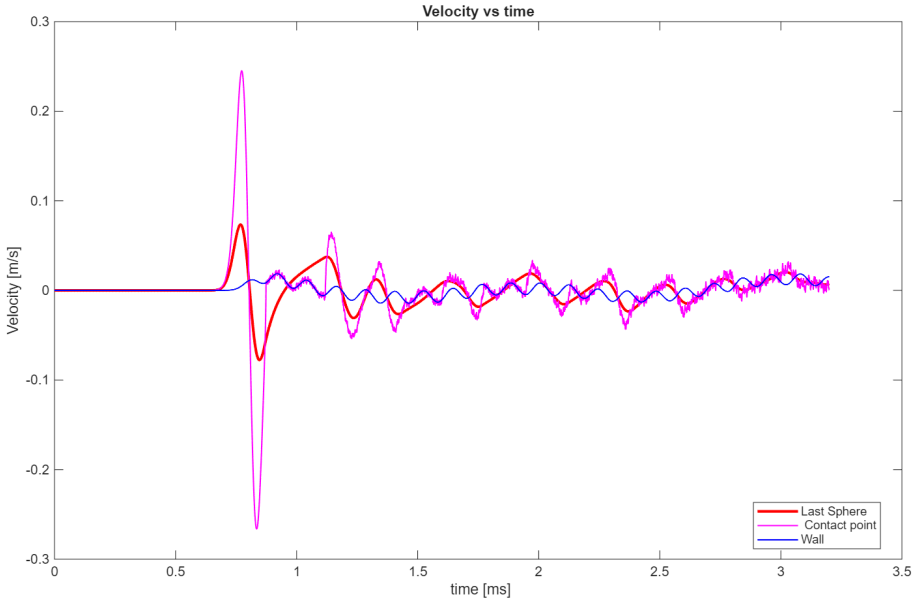

Figure 6.5: Velocities of the last sphere and the wall in the absence of damping, showing the growth of oscillations after repeated impacts.

In Fig. 6.5, the effect of the singularity at the contact point (magenta line) and the progressive growth of oscillations after each subsequent impact can be observed. Therefore, the introduction of a damping matrix is required to obtain reliable results.

For the definition of the damping matrix, a Rayleigh damping strategy was adopted.

Rayleigh damping is a method that allows the damping matrix to be expressed as a linear combination of the mass and stiffness matrices:

$$[C] = \alpha[M] + \beta[K], \tag{6.1}$$

where the coefficients α and β can be evaluated as

$$\begin{cases} \alpha = \dfrac{2(\omega_1^2\omega_2\zeta_2 - \omega_1\omega_2^2\zeta_1)}{\omega_1^2 - \omega_2^2}, \\ \beta = \dfrac{2(\omega_1\zeta_1 - \omega_2\zeta_2)}{\omega_1^2 - \omega_2^2}. \end{cases}$$

Here, ζ_1 and ζ_2 are the damping ratios associated with the natural frequencies ω_1 and ω_2, respectively.

The values of ζ_1 and ζ_2 were estimated using the half-power bandwidth method(see Appendix A).

Based on the considerations above, by selecting two reference natural frequencies, ω_1 and ω_2, and their corresponding damping ratios, ζ_1 and ζ_2, the Rayleigh damping coefficients can be determined. This approach ensures that the damping matrix

provides the desired level of damping within the frequency range defined by the selected modes, while modes at higher or lower frequencies may be over- or under-damped.

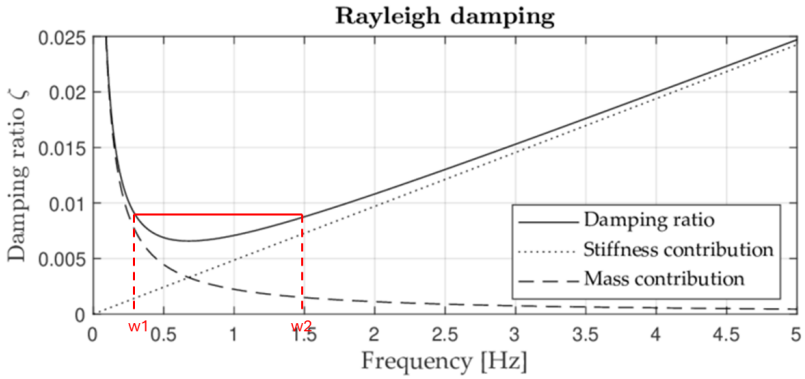

Figure 6.6: Effect of Rayleigh damping based on the reference natural frequencies ω_1 and ω_2.

For the subsequent analysis, the frequencies used to evaluate the Rayleigh damping coefficients (α and β) correspond to the lowest and highest values in the spectrum: 51 Hz and 8425 Hz. The resulting coefficients are $\alpha = 514.53$ and $\beta = 1.72e - 8$.

Chapter 7

Discussion and Validation of Results

In this chapter, the results obtained from the analysis are presented.

7.1 Energy in the system

The time evolution of the energy within the system has been evaluated in MATLAB. Before presenting the obtained results, it is important to identify the different contributions to the total energy of the system:

- Kinetic energy of the chain
- Kinetic energy of the wall
- Potential energy in the contacts
- Potential energy of the leaf springs
- Potential energy of the wall
- Dissipation energy in the contacts
- Work of the preload acting on the last sphere

At the instant (t = 0), the system is in equilibrium and the total energy of the system is given by the kinetic energy of the impactor sphere. When the first sphere collides with the chain, part of this kinetic energy is converted into potential energy stored in the contact interactions, while another part is dissipated due to damping associated with the contact interaction.

The work of the preload and the potential energy of the leaf spring, in a first approximation, have an almost negligible contribution to the total energy of the system. Conversely, the energy associated with the wall must be analyzed in greater detail, as it may provide a non-negligible contribution to the overall energy balance.

Considering all the contributions to the total energy throughout the entire contact process, the total energy should therefore be equal to the initial kinetic energy of the first sphere.

First, the interaction between the granular chain and an ideal half space is considered.

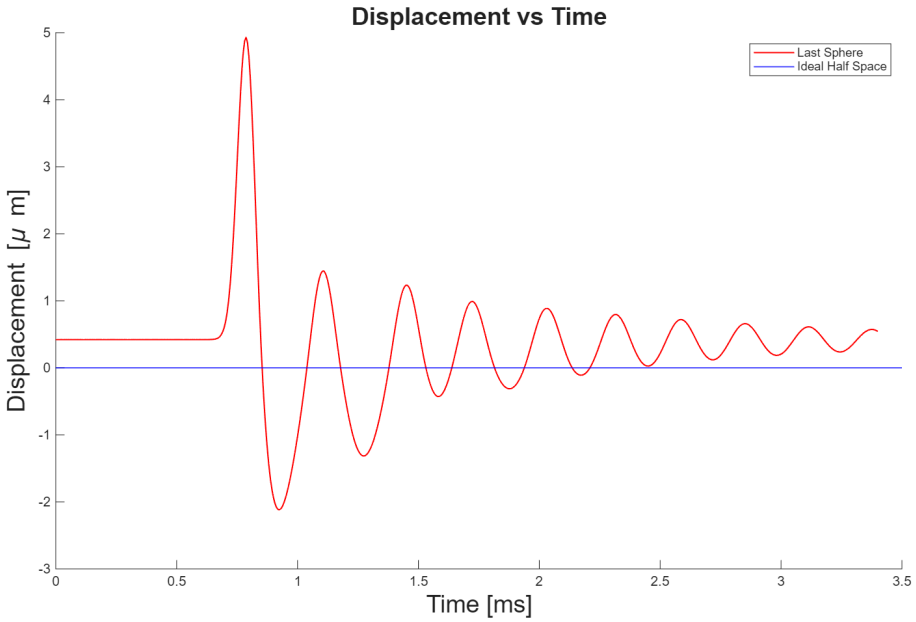

Figure 7.1: Displacements of the last sphere and the ideal half space wall

In this case, the wall does not possess any degrees of freedom and therefore cannot store energy. Consequently, the total energy of the system is given only by the contributions of the remaining components.

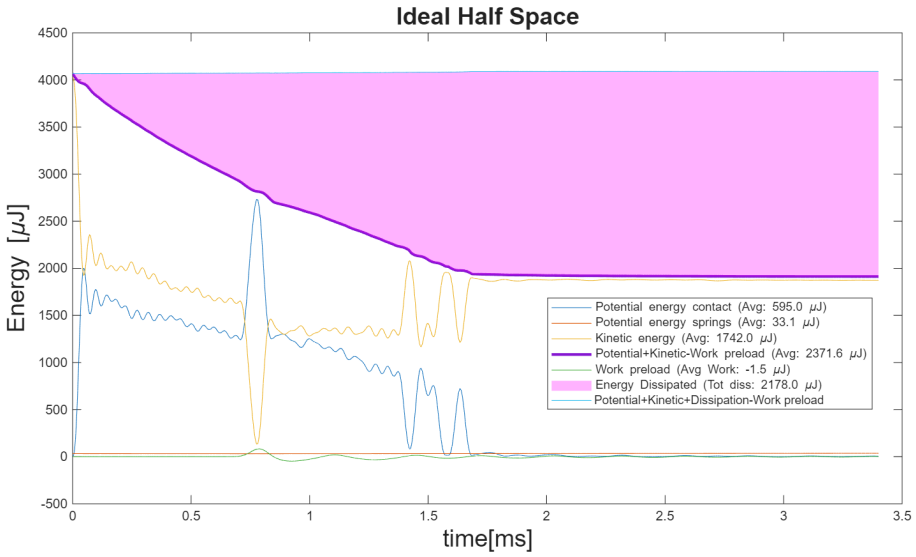

Figure 7.2: Total energy of the system for the ideal half space case

When the reduced order model (ROM) of the elastic half space is considered, the wall becomes a deformable body with its own mass and stiffness matrices.

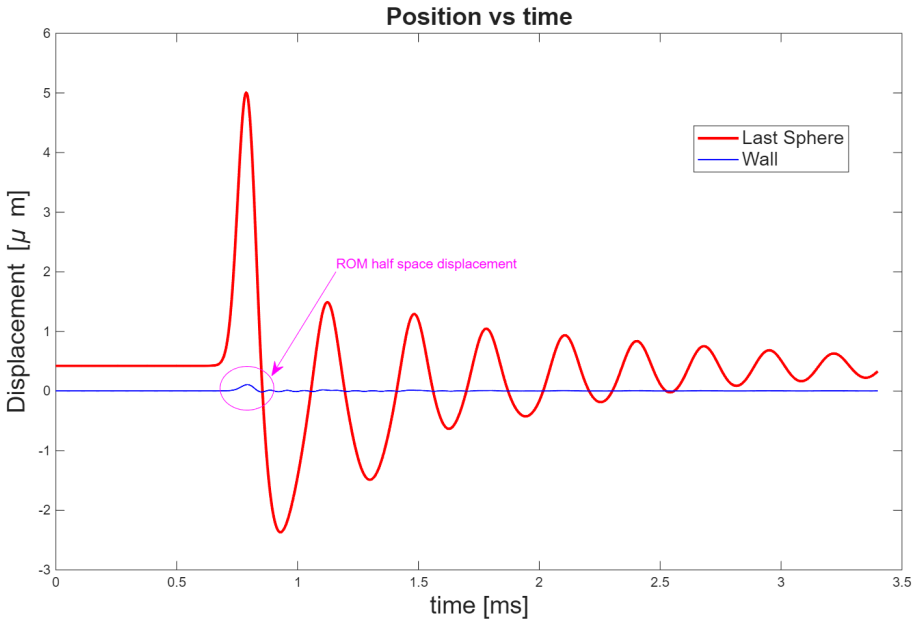

Figure 7.3: Displacement of the last sphere and the ROM half space

Part of the energy transferred by the last sphere to the elastic medium in the form of kinetic and potential energy.

However, due to the singularity in the displacement field at the contact point (see Sec.6.1), when the energy of the ROM half space is computed using the reduced mass and stiffness matrices, this additional displacement contributes to the evaluated energy, even though it does not correspond to a physical deformation of the half

space.

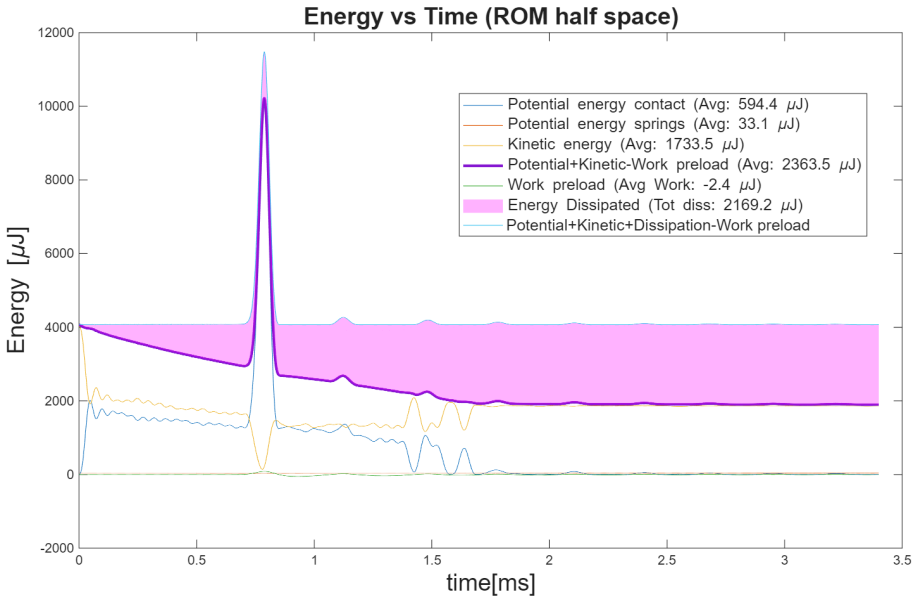

Figure 7.4: Total energy of the system for the ROM half space case

On the other hand, neglecting the energy of the wall leads to a small missing contribution in the total energy of the system.

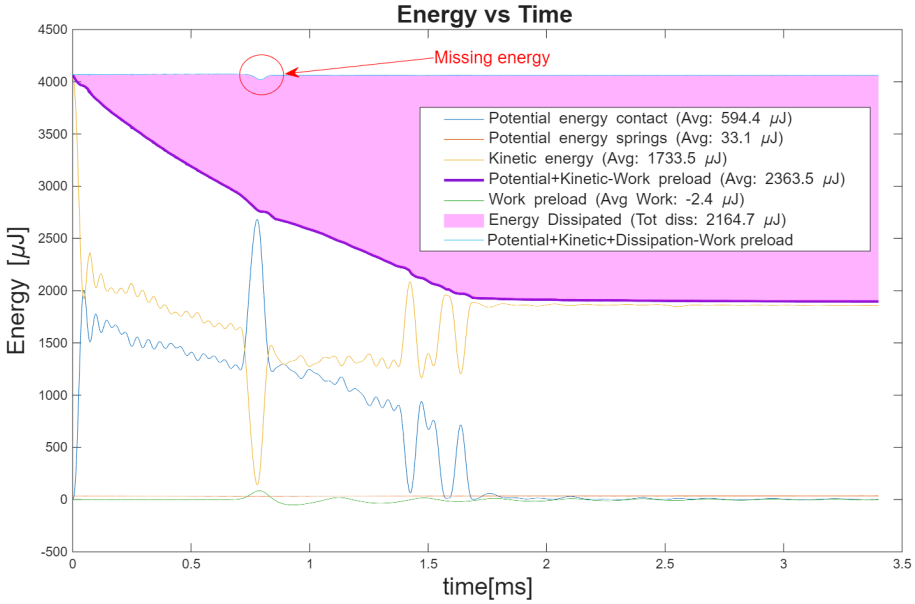

Figure 7.5: Total energy of the system without the ROM half space contribution

When the complete assembly is considered, the energy difference observed in comparison with the ROM half-space case becomes much clearer.

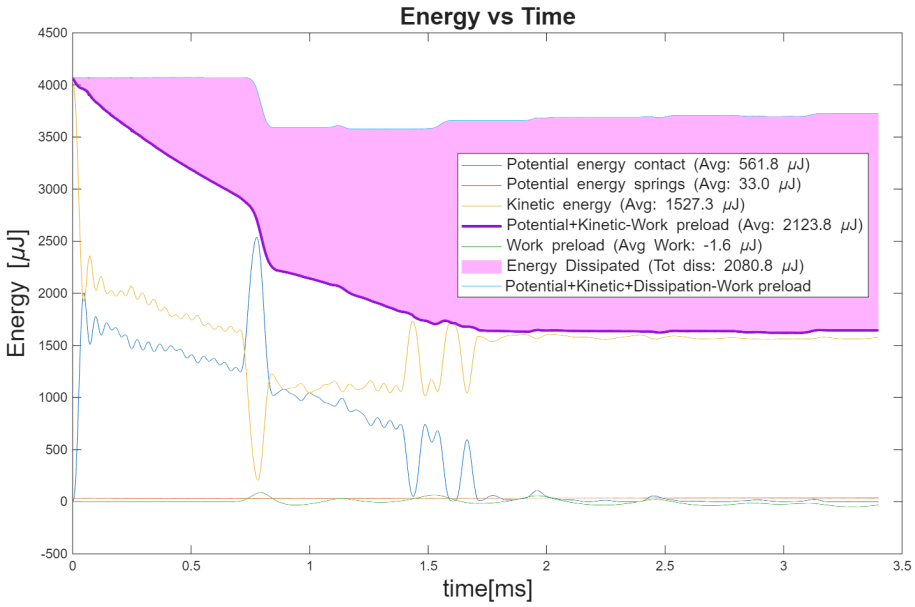

Figure 7.6: Total energy of the system without the ROM assembly contribution

This difference in behavior is due to the fact that the deformation is no longer localized only at the contact interface but also involves the dynamics of the entire assembly.

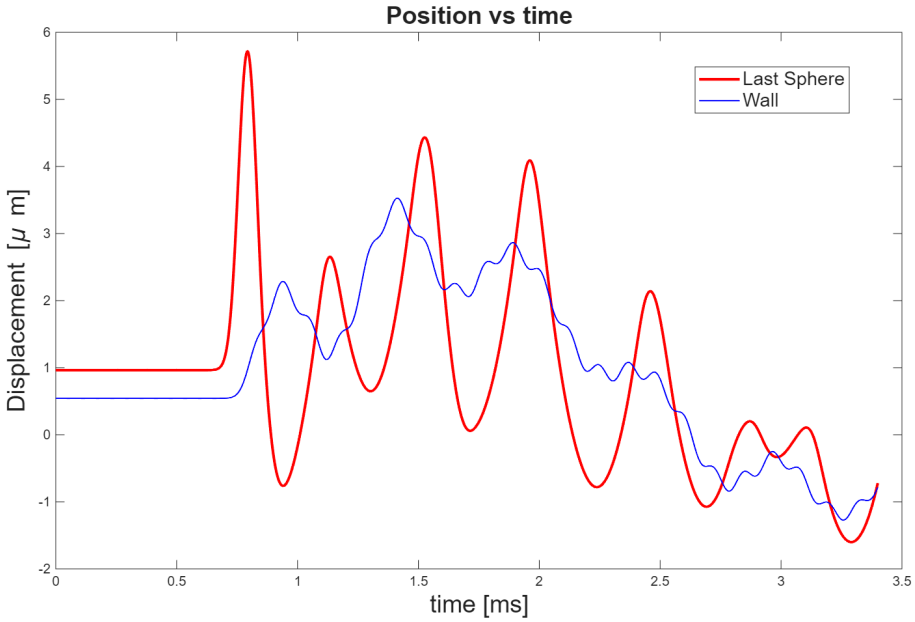

Figure 7.7: Displacement of the last sphere and the ROM assembly

However, when the kinetic and potential energy contributions of the assembly are added to the total energy of the system, the same bumps observed in Fig. 7.4 appear again.

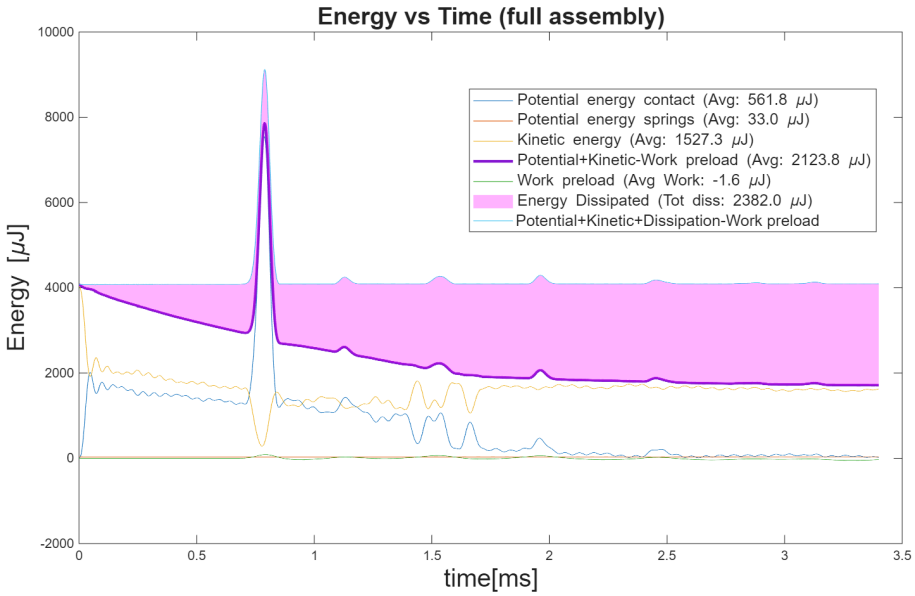

Figure 7.8: Total energy of the system for the ROM assembly case

The difference in the amplitude of the peaks between Fig. 7.4 and Fig. 7.8 is due to the different mesh size in the region surrounding the contact point in the two models.

Including the energy of the ROM wall always leads to numerical peaks at the instants when the last sphere collides with the wall. These peaks originate from the numerical singularity associated with the contact point. However, at all other times the total energy remains constant.

This observation suggests that the energy associated with the ROM wall can be interpreted as the missing energy required to recover the constant total energy observed in the ideal half-space case.

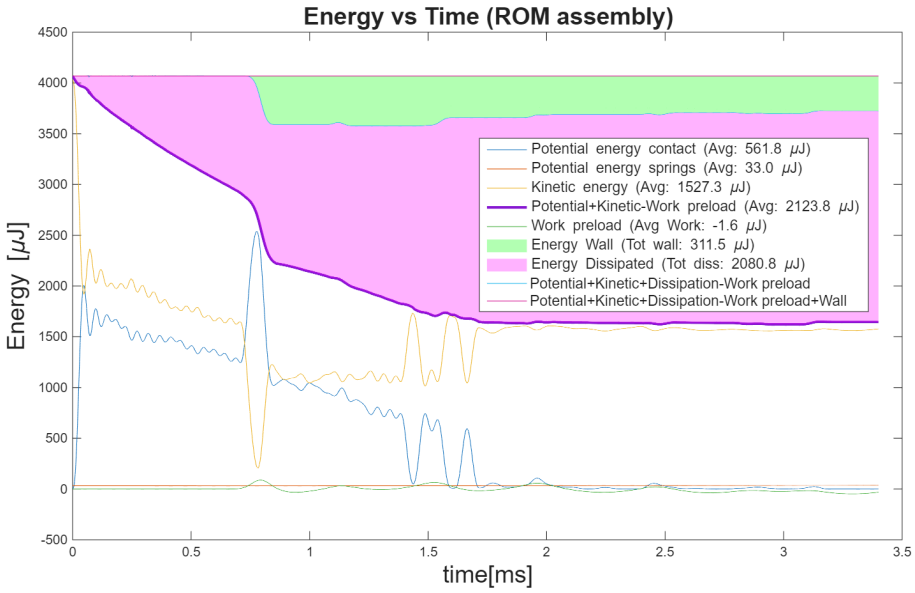

Figure 7.9: Total energy of the system

7.2 Matching Experimental results

In this section, the numerical results are compared with the experimental data obtained from the test rig presented in Chapter 3. As previously stated, it is important to emphasize that the experimental data are not the object of the present work, but are used only as a reference for the validation of the numerical model.

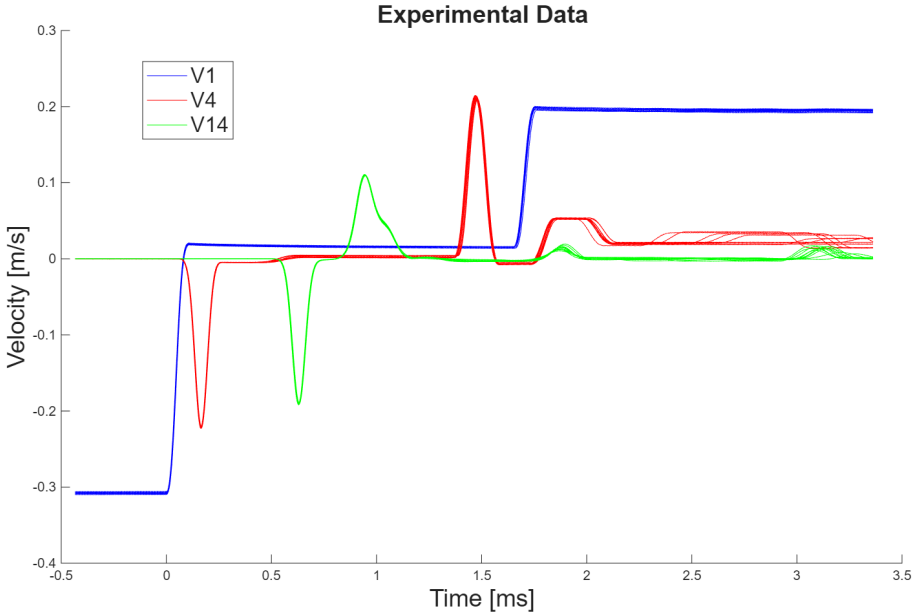

Figure 7.10: Reference experimental data

In Fig. 7.10, the 1st sphere experiences only the transit of the incident solitary

wave (SW) and of the 1st reflected solitary wave (RSW) during the time interval considered in the analysis. In contrast, the 4th sphere also experiences the transit of the 2nd and 3rd RSWs during the same time interval. The signal of the 14th sphere is additionally affected by the transit of the 4th RSW.

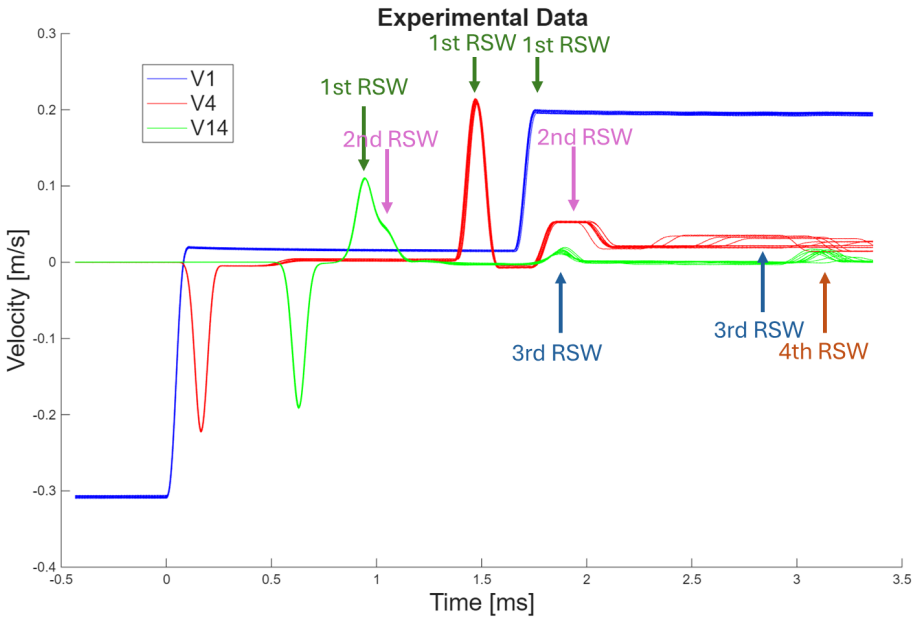

Figure 7.11: Reflected solitary waves in the experimental data

The choice of the signals from the 1st, 4th, and 14th spheres is motivated by their distance from the contact point with the wall. These locations are sufficiently far from the impact point to allow the reflected solitary waves (RSWs) to separate in time due to their different propagation velocities. As a consequence, the individual waves can be clearly distinguished in the measured signals.

If spheres located too close to the wall were considered, the different RSWs would still be partially overlapped while propagating along the chain. This would make the identification of the individual waves more difficult. The selected spheres therefore provide signals in which the solitary waves are sufficiently separated while still representing a representative sample of the chain response, allowing a reliable validation of the experimental behavior.

In Fig. 7.10, the experimental data for each sphere consist of ten signals.

Before proceeding, it is important to clarify that, up to this point, the spheres in the chain have been assumed to be perfectly elastic. However, several experimental tests performed over time have shown that, due to the high contact pressures generated by Hertzian contacts, some plastic deformation occurs, mainly in the last sphere. This can happen even for relatively low initial velocities of the impactor

sphere (in the present work the initial velocity is around 0.31 m/s).

Although the Hertzian contact between two spheres produces a smaller contact area and therefore a higher maximum pressure for the same applied force, the last contact in the chain experiences the largest contact force. This occurs because the compression wave propagating through the chain is reflected at the rigid boundary, concentrating the force at the sphere–wall interface. As a result, the maximum Hertzian pressure at the last contact can exceed the yield limit of the material, leading to plastic deformation.

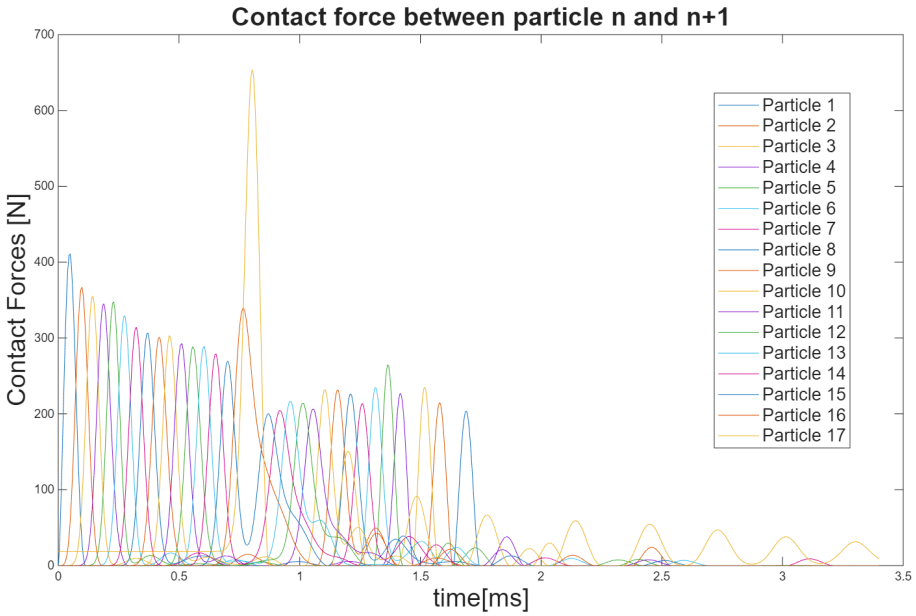

Figure 7.12: Contact force history

To account for this phenomenon, the stiffness of the last contact was increased by a factor of 3, following the approach suggested in [2].

The comparison between the numerical predictions and the experimental data is now performed.

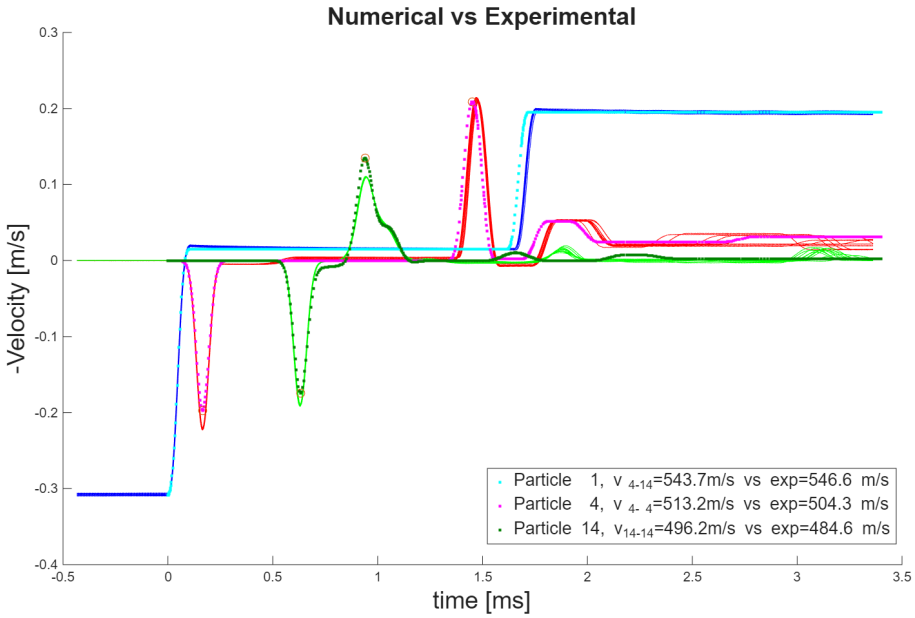

Figure 7.13: Comparison numerical half space solution vs experimental data

In Fig. 7.13, the dotted lines represent the numerical solution whereas the solid lines represent the experimental data.

The numerical results for the half space case in Fig.7.13, well approximate the experimental data for the incident SW for each of the three spheres and for the 14th spheres also the 1st and the 2nd RSWs are matched. However, both of the RSWs for the 4th and 1st spheres differ from experimental data in terms of velocity of the waves. Moreover, the most significant mismatch appears for the 3rd and the 4th RSWs.

For these reasons, the model of the wall as half space, is not accurate for describing the dynamics of the system. Therefore, the wall is now modeled as single Degree of Freedom (1 DOF).

The value of the mass and of the stiffness for the 1 DOF wall can be tuned in order to simulate, one at a time, the frequencies of the assembly in Fig.5.1.

It is important to specify that, as shown in Fig. 5.1, the first modal shape of the assembly at 51 Hz occurs mainly in the tangential direction and therefore slightly influences the reflected solitary waves. For this reason, only the frequencies of 269 Hz, 907 Hz, and 8425 Hz are considered.

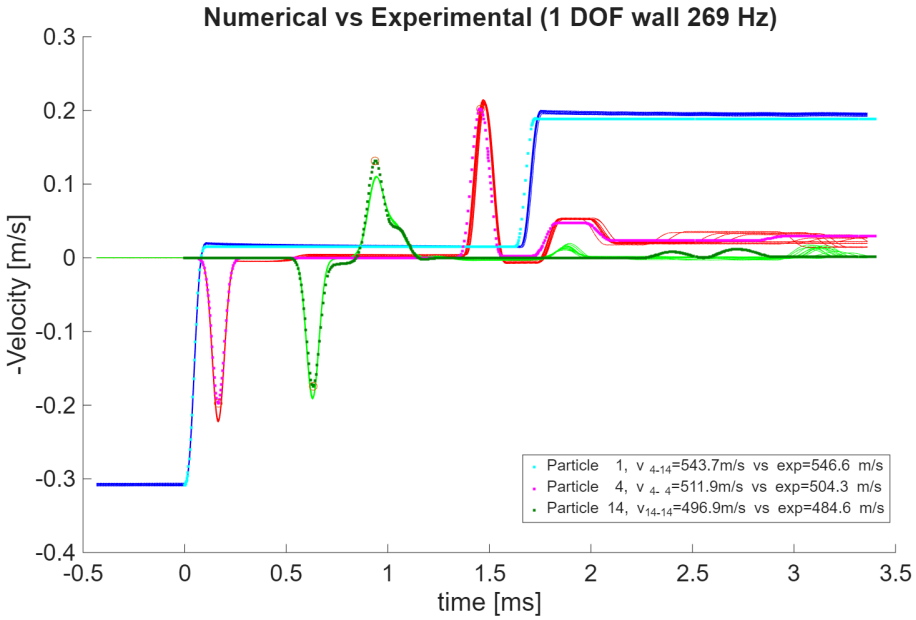

(a) 269 Hz

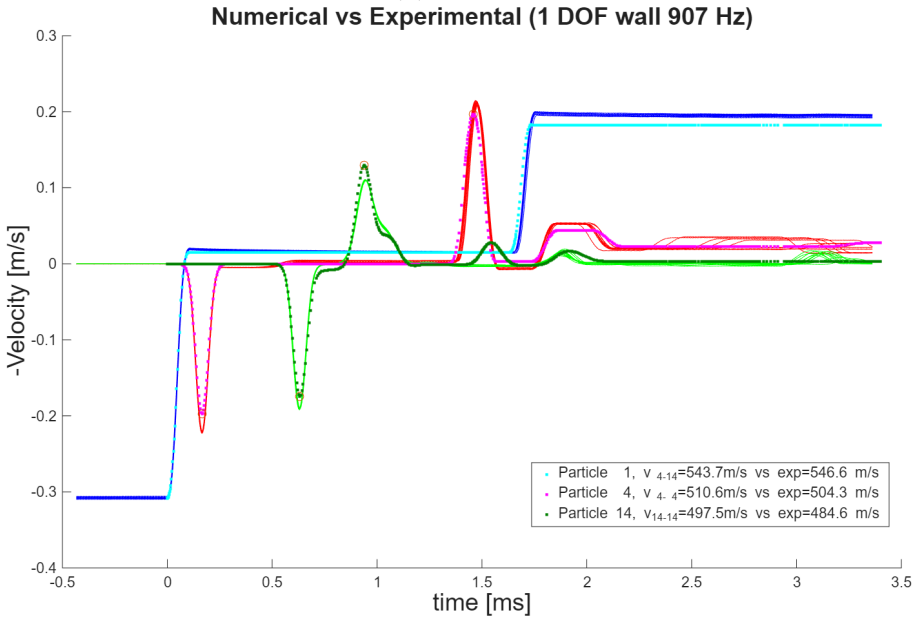

(b) 907 Hz

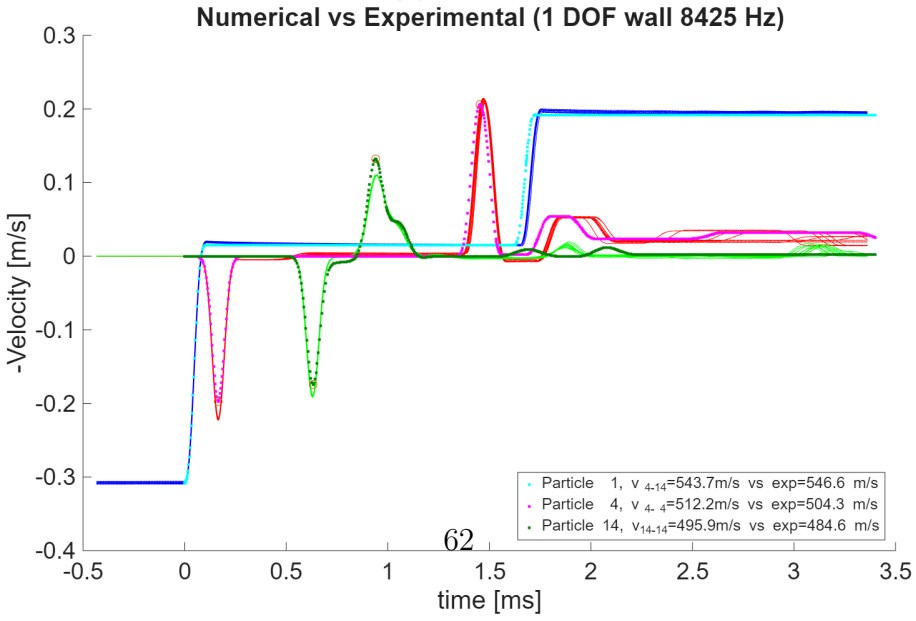

(c) 8425 Hz

The comparison with the experimental data in Fig. 7.14a and Fig. 7.14b shows a slightly improved agreement in terms of the 2nd RSW for the 4th sphere. However, the 3rd and 4th reflections still remain unmatched by the numerical model.

For a high modal frequency, such as 8425 Hz in Fig. 7.14c, it can be observed that, since a higher frequency corresponds to a higher stiffness value, the results are similar to those obtained for the half-space case.

The 1 DOF wall models have been analyzed; however, none of the considered wall dynamics provides a satisfactory match with the experimental data. For this reason, the Reduced Order Model (ROM) walls are now analyzed.

As described in Sec. 5.2, the 2nd and 3rd modal shapes of the assembly conflict with each other when defining the most suitable configuration for the assembly dynamics. Therefore, two different ROM models of the assembly are considered. Each model matches three of the four main modal shapes of the assembly.

In the following analysis, the ROM wall that matches the modal shapes at 51, 269, and 8425 Hz will be referred to as *ROM 269*, whereas the ROM wall that matches the modal shapes at 51, 907, and 8425 Hz will be referred to as *ROM 907*.

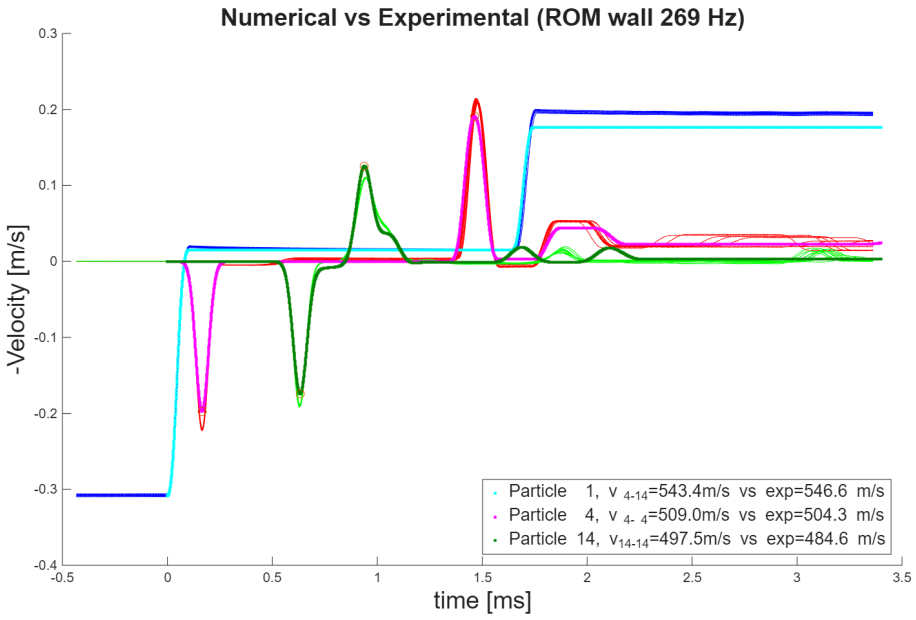

Figure 7.15: ROM wall matching the modal shape at 269 Hz

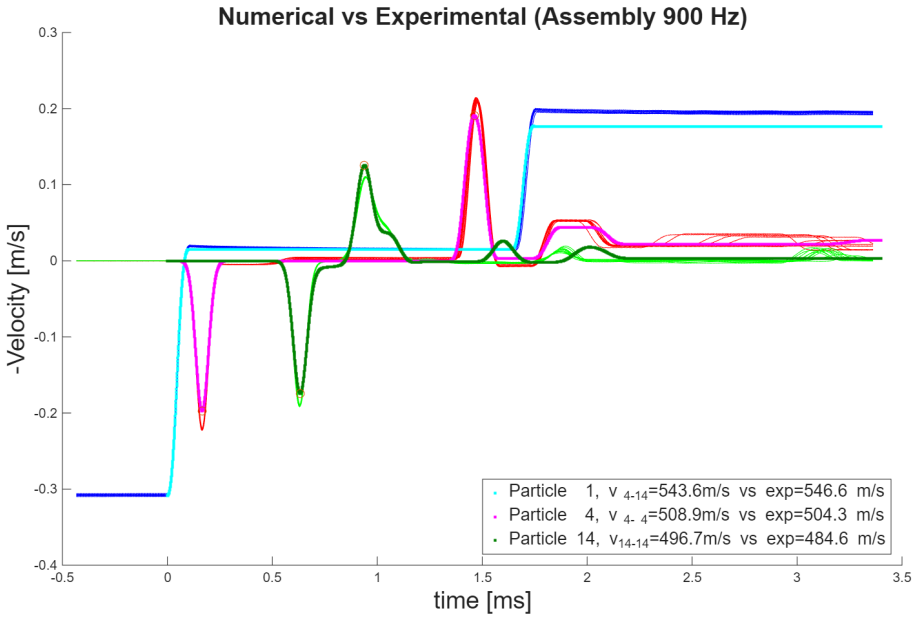

Figure 7.16: ROM wall matching the modal shape at 907 Hz

From the results shown in Fig. 7.15 and Fig. 7.16, several observations can be made.

First, the results obtained with the ROM 907 show a behavior that is overall consistent with the one obtained using the 1 DOF wall tuned at the frequency of 907 Hz. Although some differences are still present, particularly in the 3rd and 4th reflected solitary waves (RSWs), the general trend of the signals is similar in the two models.

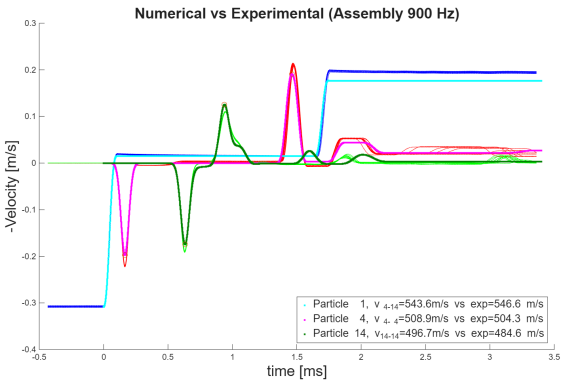

ROM 907 Hz results

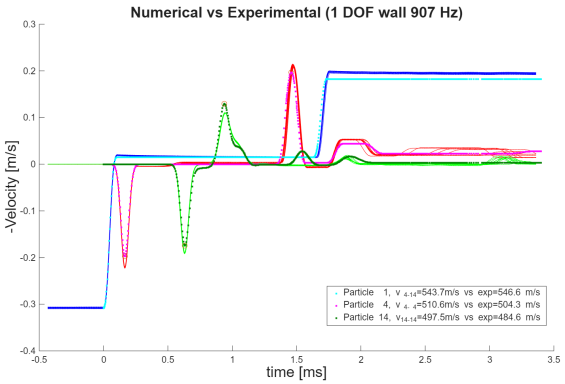

1 DOF 907 Hz results

In contrast, the results obtained with the ROM 269 differ significantly from those obtained with the corresponding 1 DOF model tuned at 269 Hz.

However, it can be observed that the ROM 269 mode predicts the higher-frequency mode, which should occur around 907 Hz, at approximately 700 Hz. Interestingly, the response of this ROM model shows a behavior similar to that

obtained with a 1 DOF model tuned at 700 Hz. This suggests that the dynamic response of the system is strongly influenced by this higher-frequency mode.

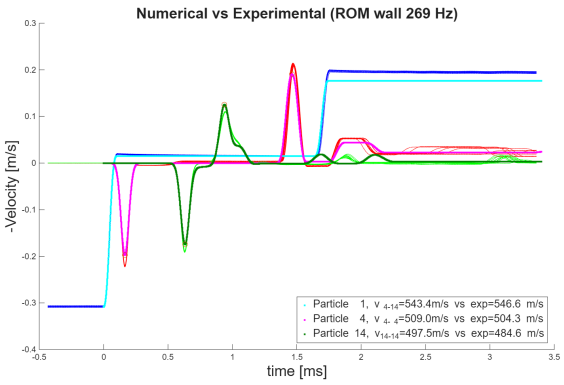

ROM 269 Hz results

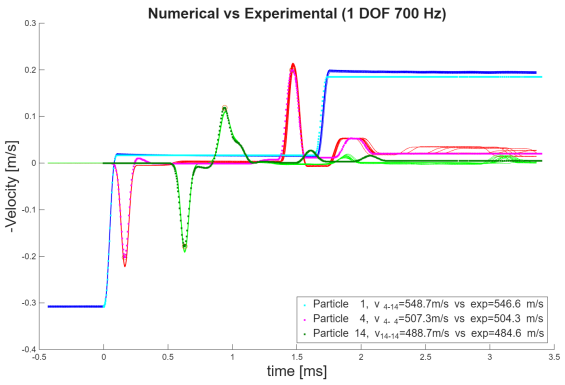

1 DOF 700 Hz results

These observations indicate that the modal shape associated with the frequency of 907 Hz, i.e., the torsional mode of the sheets, represents one of the dominant modes governing the interaction between the chain and the wall, and therefore has a major influence on the overall wave dynamics.

However, the lower-frequency mode at 269 Hz still plays a role in the system response. In particular, it affects the temporal separation of the higher-order reflected solitary waves.

After these analyses, none of the wall models appears suitable to accurately capture the dynamics of solitary waves in the system, leaving the experimental data unmatched.

However, what results clear in this analysis is that the incident SW and the 1st RSW are completely independent from the dynamics of the assembly since when the first impact between the chain and the wall occurs, the assembly is in rest conditions. The 2nd RSW is slightly dependent from the wall behaviour and mainly it can be observed in the 4th sphere. Therefore, the wall dynamics is important from the 3rd and the 4th reflection.

For this reasons, the system was optimized to capture the dynamics of solitary waves determined exclusively by the chain properties.

7.3 Optimization

As discussed in the previous section, the contact chain of the actual test rig is not ideal. Phenomena such as wear, plastic deformation, and imperfect alignment of the

chain can significantly affect the experimental results. For this reason, the Hertzian contact stiffness (Ai) may slightly differ from contact to contact.

To account for these uncertainties, an optimization procedure was implemented in Matlab. The optimization code uses the function fmincon to iteratively solve the system ODE while varying the contact stiffness parameters (Ai).

The optimization minimizes the residual between the experimentally measured solitary waves and the numerical predictions. Only solitary waves that are independent of the wall interaction were considered in this stage, since they depend solely on the properties of the granular chain.

The calibrated chain model is used as the baseline configuration.

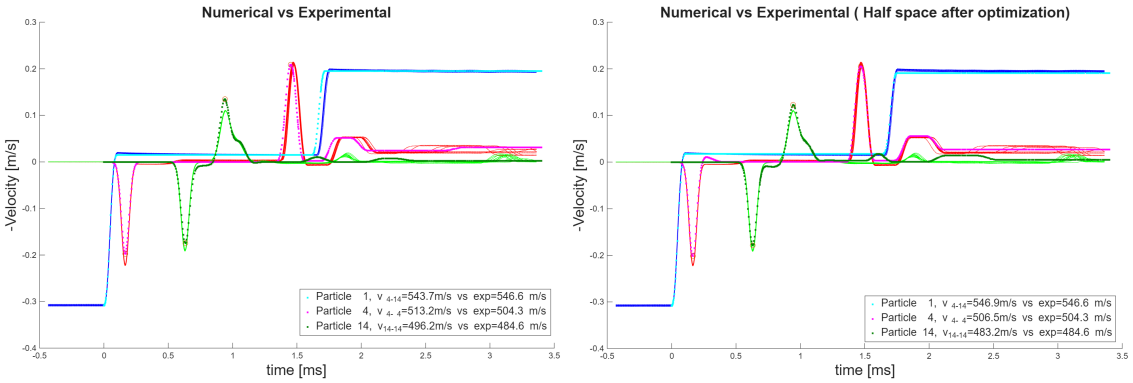

Elastic Half Space | Elastic Half Space after optimization

Figure 7.17: Comparison Half Space results before and after optimization

From Fig. ??, it is evident that after the optimization the numerical results show a better agreement with the experimental data. However, the Half-Space model still remains unsuitable for accurately describing the third and fourth reflected solitary waves (RSWs).

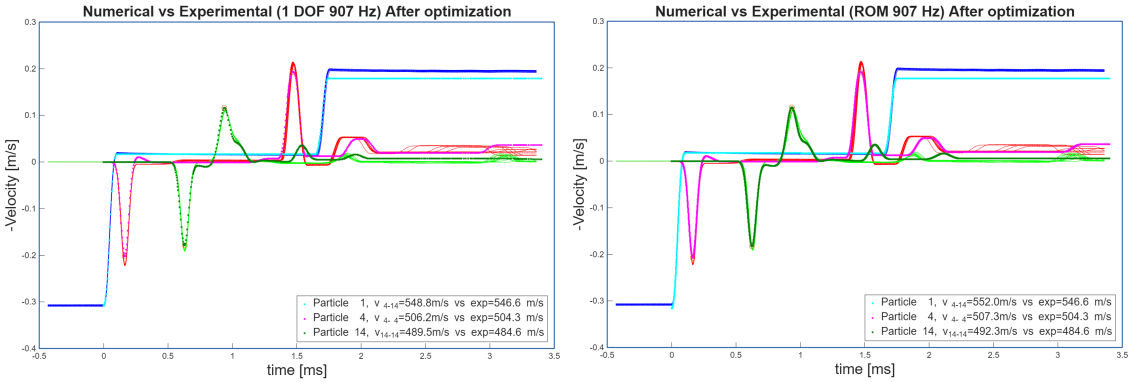

1 DOF 907 Hz after optimization | ROM 907 Hz after optimization

Figure 7.18: Comparison 1 dof and ROM walls results after optimization

This figure shows that, as previously demonstrated, the mode at 907 Hz has the largest influence on the results. However, both models still appear unsuitable for accurately describing the wall dynamics.

However, the strong similarity between the predictions of the two models suggests that the wall dynamics can be effectively represented by a simplified 1-DOF model, without necessarily resorting to the reduced-order model (ROM), as both approaches provide comparable results.

Consequently, instead of directly adopting one of the natural frequencies identified in the structural model, the natural frequency of the 1-DOF system was treated as an effective parameter and tuned to improve the agreement with the experimental measurements. This procedure led to an optimal frequency of 240 Hz, which does not correspond to any specific structural mode of the wall but rather represents an equivalent dynamic response of the system.

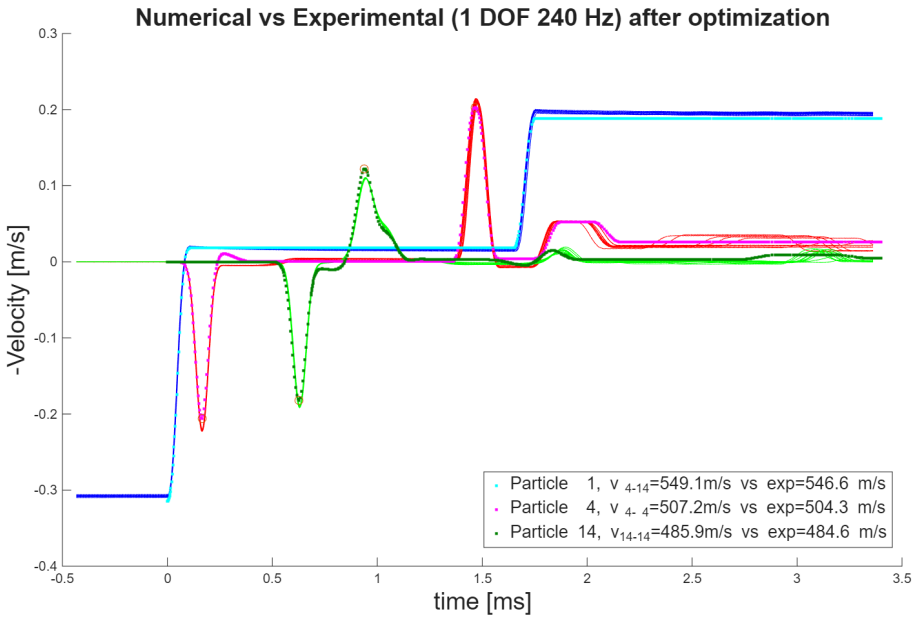

Figure 7.19: Comparison between experimental data and calibrated 1-DOF model with equivalent natural frequency of 240 Hz

As shown in Fig. 7.19, the calibrated model exhibits excellent agreement with the experimental results, accurately reproducing the observed behavior. This confirms that the simplified 1-DOF representation is able to capture the dominant dynamics of the wall.

Chapter 8

Conclusions and Future Work

8.1 Conclusions

The objective of this work is to numerically investigate the propagation of solitary waves in granular chains interacting with a frictional boundary, and to assess the effect of different boundary models on the resulting wave response. The simulations are validated against existing experimental data obtained from a test rig developed at the University of Illinois at Urbana–Champaign.

First, an existing MATLAB code for the simulation of solitary wave propagation was successfully updated. The improved implementation allows the selection of different boundary conditions, enabling the boundary to be modeled using several approaches, namely an elastic Half-Space, a single degree-of-freedom (1-DOF) system, and a Reduced Order Model (ROM). This modification provides greater flexibility in the numerical investigation of wave–boundary interactions.

The Half-Space model provides a good first approximation of the boundary behavior, as it captures the first and second reflected solitary waves (RSWs) with good agreement with the experimental observations. However, for a more detailed analysis, discrepancies remain in the third and fourth RSWs, which are not fully reproduced by this model.

The 1-DOF model represents a powerful and flexible approach, as it allows the dynamic behavior of the boundary to be tuned through its parameters. However, in its initial configuration, the model was not able to accurately reproduce the third and fourth reflected solitary waves observed in the experimental results.

The Reduced Order Model (ROM) was developed using the modal properties obtained from hammer tests performed on the experimental setup. Numerical simulations indicate that the torsional mode at approximately 900 Hz is the dominant one within the considered frequency range. The ROM successfully reproduces three

of the four main natural frequencies experimentally identified for the block. However, it was found to be unsuitable for accurately describing the dynamic interaction between the granular chain and the wall.

This limitation is mainly attributed to the fact that only the modal properties of the block were included in the reduced model. The dynamic behavior of the connection between the assembly and the supporting table, as well as the vibration modes of the table itself, were not considered. These effects can significantly influence the overall system response and should therefore be included in future modeling efforts.

Despite this, the Reduced Order Model proved useful for interpreting the dynamic response of the system. In particular, the good agreement obtained with the 1-DOF model supports its validity in describing the wall dynamics and reproducing the experimental results.

Finally, the experimental results were successfully reproduced by the numerical model by adopting a tuned 1-DOF boundary model with a natural frequency of 240 Hz.

Overall, the agreement between the numerical and experimental solitary waves confirms the consistency of the experimental measurements and the validity of the developed numerical framework. While the Reduced Order Model represents the most physically representative approach for describing the boundary dynamics, its current implementation remains incomplete and should be further improved to properly account for the dynamics of the supporting structure. In contrast, the tuned 1-DOF model proved to be an effective and practical alternative, providing a good compromise between computational efficiency, modeling flexibility, and accuracy in reproducing the experimental results.

8.2 Future Works

Future work should focus on further improving the modeling of the system. A first step would be to investigate the influence of the vibration modes of the supporting table in the Reduced Order Model, since the interaction between the assembly and the support structure may significantly affect the dynamic response.

Moreover, considering the high sensitivity of solitary wave propagation to contact conditions, it would be interesting to describe the contact interactions more accurately. One possible approach would be to model the contacts between the spheres using a finite element formulation to better capture local contact dynamics, potentially employing advanced frictional contact algorithms for higher-order elements [10].

The code developed in the present work can serve as a foundation for modeling and simulating a new test rig currently being developed at Imperial College, which aims to explore the use of solitary waves for frictional interfaces.

Building on this foundation, the ultimate goal of this research is the development of a device for non-destructive evaluation (NDE) based on the propagation of solitary waves. The results obtained in this work confirm that solitary waves are a powerful tool for this type of application. However, their response can be influenced by several factors, and further investigations are therefore required to fully understand and control these effects.

Appendices

A Appendix: Half-Power Bandwidth

From the experimental tests, a Frequency Response Function (FRF) of the wall dynamics was obtained. Consequently, after applying the Fourier transform, the resonance peaks of the signal were identified. These peaks correspond to the natural frequencies of the assembly.

To estimate the damping ratio associated with each peak, which corresponds to a modal shape of the assembly, the half-power bandwidth method can be implemented.

For the characterization of the FRF peaks, the following quantities are defined:

- f_n: the frequency at which the peak occurs, representing the position of the peak on the x-axis.
- $A_{\max}$: the amplitude of the peak, identified on the y-axis.

Given the amplitude $A_{\max}$, two frequencies, f_1 and f_2, can be defined where the amplitude is equal to $A_{\max}/\sqrt{2}$. This value corresponds to the half-power point, i.e., the amplitude at which the power is half of the peak power. These two frequencies represent the lower and upper bounds of the half-power bandwidth region.

The knowledge of f_1 and f_2 allows the calculation of the damping ratio ζ using the relation:

$$\zeta = \frac{f_2 - f_1}{2f_n}. \tag{1}$$

Bibliography

[1] Alfredo Fantetti. Experimental characterization of frictional hysteresis for non-linear dy namic analysis of jointed structures. February 2022.

[2] K. L. Johnson. *Contact Mechanics*. Cambridge University Press, Cambridge, 1985.

[3] D. Khatri L. De Nardo C. Daraio J. Yang, C. Silvestro. Interaction of higly nonlinear solitary waves with linear elastic media. *Physical Review E*, E83, 2011.

[4] D.M. McFarland K. Remick L.A. Bergman A.F. Vakasis R. Potekin, K.R. Jayaprakash. Experimental study of strongly nonlinear resonances and anti-resonances in granular dimer chains. *Experimental Mechanics*, 53:861–870, 2013.

[5] V. F. Nesterenko. *Dynamics of Heterogeneous Materials*. Springer-Verlag, New York, 2001.

[6] S. Fauve E. Falcon, C. Laroche and C.Coste. Collision of a 1-d column of beads with a wall. *The European Physical Journal*, B5:111–131, 1998.

[7] S. Fauve E. Falcon, C. Laroche and C.Coste. Behaviour of one inelastic ball bouncing repeatedly off the ground. *The European Physical Journal*, B3:45–57, 1998.

[8] P.Anzel C. Daraio J. Yang, D. Khatri. Interaction of higly nonlinear solitary waves with thin plates. *International Journal of Solid Structures*, 49:1463–1471, 2012.

[9] Mason A. Porter P.G. Kevredikis R. Carretero-Gonzàlez, D. Khatri and C. Daraio. Dissipative solitary waves in granular crystals. *Physical Review Letters*, 2009.

[10] Nik Petrinic Indrajeet Sahu. Unbiased higher-order frictional contact using midplane and patch based segment-to-segment penalty method. *Computational Mechanics*, 2025.